Noninvasive embedding of single Co atoms in Ge(111)2 × 1 surfaces

D. A. Muzychenko,[1,*] K. Schouteden,[2,†] M. Houssa,[3] S. V. Savinov,[1] and C. Van Haesendonck[2]
[1]*Faculty of Physics, Moscow State University, 119991 Moscow, Russia*
[2]*Laboratory of Solid-State Physics and Magnetism, KULeuven, BE-3001 Leuven, Belgium*
[3]*Semiconductor Physics Laboratory, Department of Physics and Astronomy, KULeuven, BE-3001 Leuven, Belgium*
(Received 7 September 2011; revised manuscript received 6 January 2012; published 12 March 2012)

We report on a combined scanning tunneling microscopy (STM) and density functional theory (DFT) based investigation of Co atoms on Ge(111)2 × 1 surfaces. When deposited on cold surfaces, individual Co atoms have a limited diffusivity on the atomically flat areas and apparently reside on top of the upper π-bonded chain rows exclusively. Voltage-dependent STM imaging reveals a highly anisotropic electronic perturbation of the Ge surface surrounding these Co atoms and pronounced one-dimensional confinement along the π-bonded chains. DFT calculations reveal that the individual Co atoms are in fact embedded in the Ge surface, where they occupy a quasistationary position within the big 7-member Ge ring in between the third and fourth atomic Ge layer. The energy needed for the Co atoms to overcome the potential barrier for penetration in the Ge surface is provided by the kinetic energy resulting from the deposition process. DFT calculations further demonstrate that the embedded Co atoms form four covalent Co–Ge bonds, resulting in a Co^{4+} valence state and a $3d^5$ electronic configuration. Calculated STM images are in perfect agreement with the experimental atomic resolution STM images for the broad range of applied tunneling voltages.

DOI: 10.1103/PhysRevB.85.125412 PACS number(s): 68.43.Fg, 68.47.Fg, 68.37.Ef, 81.07.Ta

I. INTRODUCTION

The continuous miniaturization of electronic circuits has resulted in the emergence of novel classes of nanometer-size devices that rely on the quantum-mechanical nature of charge carriers.[1,2] Examples of state-of-the-art nanodevices can be found in molecular electronics[3–5] and spintronics.[6] The dimensions of the active elements, connections, and separations are now being reduced to the order of a few atomic rows and, in the ultimate limit, devices may be built up using atomic-size elements[7,8] that are connected by atomic nanowires. However, to fulfill the demands related to the never ceasing development of electronics, novel materials with electronic properties superior to those of the currently used silicon are required. Among all candidates germanium is considered one of the most promising alternative materials[9,10] because it allows higher switching speeds due to a lower effective hole mass and a higher electron and hole drift mobility.[11] This makes germanium ideally suited for use in ultrafast complementary metal-oxide-semiconductor technology, in particular for metal-oxide-semiconductor field-effect transistors[12–14] and band-to-band tunneling field-effect transistors.[15] For this purpose detailed investigations of the electronic properties of dopants and defects or metal alloys in Ge crystals are obviously required.[16]

One of the major challenges for future nanoelectronic applications is the controlled preparation of low-dimensional structures on semiconductor surfaces, e.g., quantum dots[17] and quantum wires.[18–20] Due to their broad range of electronic and magnetic properties, such nanostructures are ideal model systems for the fundamental study of low-dimensional physics as well as for the exploration of new device concepts[21] that also exploit the spin character of the charge carriers.[6,22,23]

Within this context, deposition of metal atoms on Ge surfaces has attracted considerable scientific interest during recent years, since it was found that atoms of different materials self-organize into different types of nanostructures after deposition on Ge. It has been demonstrated that deposited Mn atoms do not coagulate on Ge(111)$c2 \times 8$ surfaces in the initial adsorption stage, yielding zero-dimensional (0D) structures on Ge(111).[24,25] On the other hand Pt,[26–30] Au,[31,32] and Sn atoms[33] spontaneously form one-dimensional (1D) atomic chains on Ge(001), whereas Pd[34,35] and Ag[36,37] atoms favor the formation of two-dimensional (2D) or three-dimensional (3D) particles on Ge(001).

The emerging field of spintronics requires (self-)assembly of nanostructures with well-defined magnetic properties on semiconducting surfaces. Due to the high spin polarization of the charge carriers near the Fermi level, Co is one of the most important elements used in magnetic recording media as well as in giant magnetoresistance devices.[38] Recently, the electronic and magnetic behaviors of ultrathin ($\leqslant$5 monolayers) Co/Ge[39–43] and Co/Ag/Ge[44–46] films have been investigated. The initial adsorption stage of single Co atoms on Ge surfaces has not been studied so far. Thorough knowledge of the formation process of the Co/Ge interface during the first adsorption stages is, however, of crucial technological and fundamental interest.

Here, we present a comprehensive study of the initial growth stages of Co on 2 × 1 reconstructed Ge(111) by means of low-temperature (LT) scanning tunneling microscopy (STM) and spectroscopy (STS), combined with first-principles density functional theory (DFT) calculations within the local-density approximation. STM and STS are ideal tools to investigate with high spatial and energy resolution the surface reconstruction and the local electronic properties of the Ge(111) surface after adsorption of individual Co atoms. DFT calculations on the other hand allow us to predict the electronic properties of systems of up to thousands of atoms in size. High-resolution STM and STS combined with DFT hence provide a powerful tool for the investigation of atomic-size systems. Here, we report on the experimental observation of "noninvasive embedding" (i.e., without destroying the surface reconstruction) of individual Co atoms in the Ge(111)2 × 1 surface and on the formation of larger Co/Ge intermixed layers

after Co deposition on the cold ($T_{\text{sample}} \leqslant 80$ K) Ge(111)2 × 1 surface. The location of an individual Co atom in the Ge surface, its influence on the surrounding Ge atoms, and the resulting electronic properties are systematically investigated. Voltage-dependent STM imaging reveals a highly anisotropic electronic perturbation of the Ge surface surrounding the Co atom, which is accompanied by pronounced 1D confinement along the π-bonded chains. Our experimental findings are well explained by the detailed DFT calculations.

II. INSTRUMENTATION

STM and STS measurements were performed with a LT STM setup (Omicron Nanotechnology), operating at a base pressure in the 10^{-11} mbar range. All data were acquired at $T_{\text{sample}} \simeq 4.5$ K. Electrochemically etched W tips were cleaned *in situ* by repeated flashing well above 1800 K to remove the surface oxide layer and any additional contamination. The tip quality was routinely checked by acquiring atomic-resolution images of the "herringbone" reconstruction of the Au(111) surface.[47,48] STM topographic imaging was performed in constant-current mode. The tunneling voltages V_t indicated in the text and figure captions are with respect to the sample (the STM tip is virtually grounded). Image processing was performed by Nanotec WSxM.[49]

Ge single crystals with a resistivity of $\rho_{\text{bulk}} \simeq 0.2\ \Omega$cm were doped with Ga at a doping level of $n_{\text{Ga}} = 1$ to 2×10^{16} cm^{-3}, resulting in p-type bulk conductivity. $4 \times 1.5 \times 0.8$ mm^3 Ge bars, with their long axis aligned with the (111) direction, were cleaved *in situ* at room temperature in the sample preparation chamber at a pressure of around 5×10^{-11} mbar. The freshly cleaved samples were transferred within about 5 minutes to the STM measurement chamber. The pressure in the STM measurement chamber was about 4×10^{-12} mbar during the LT STM measurements. Under these conditions the cleaved Ge surfaces were observed to retain their cleanliness for 5 to 7 days. This way, we have investigated 7 freshly cleaved Ge(111) crystals.

After checking the freshly cleaved Ge(111)2 × 1 sample in the STM measurement chamber, 0.02 to 0.04 monolayers of Co were deposited on the cold Ge(111)2 × 1 surface ($T_{\text{sample}} \leqslant 80$ K) in the sample preparation chamber. Deposition was achieved by evaporation from a high-purity Co (99.9996%) rod with an e-beam evaporator, at pressures below 10^{-10} mbar and at a low deposition rate of around 0.007 ± 0.001 monolayers (MLs) per second. After Co deposition, the Ge(111)2 × 1 sample was transferred immediately to the LT STM measurement chamber. Overall transport time, including deposition time, was around 25 minutes. Here we focus on the results obtained on 4 different Co/Ge(111)2 × 1 samples for which 2.1 μm^2 atomic resolution STM topography images were recorded and analyzed.

III. EXPERIMENTAL RESULTS

A. Topography and electronic structure of the freshly cleaved Ge(111)2 × 1 surface

The 2 × 1 reconstruction of the Ge(111) surface consists of π-bonded chains of Ge atoms running in the [01$\bar{1}$] direction.[50–52] Only every other (upper chain) row can be imaged by STM.[53] The surface unit cell contains two atoms,

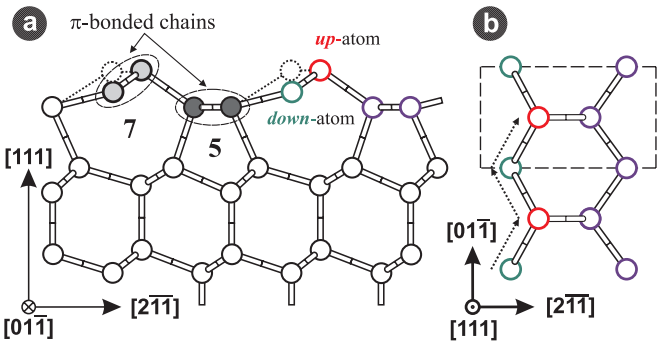

FIG. 1. (Color online) (a) Schematic side view of the chain-left isomer of the 2 × 1 reconstruction of the Ge(111) surface according to the original Pandey π-bonded chain model (dotted lines) and including the effect of buckling (solid lines) (Ref. 50). The 7-member and 5-member Ge rings of the surface reconstruction are indicated by the numbers 7 and 5, respectively. (b) Schematic top view of "zigzag" chain structure of the three top layers in (a). The dashed frame indicates the surface unit cell, while the arrows with dotted lines indicate the "zigzag" structure of the upper π-bonded chain along the [01$\bar{1}$] direction.

both having one dangling bond. This dangling bond is responsible for π bonding along the upper surface chain rows (see Fig. 1). In the original Pandey geometry,[51] the two upper atoms of the 7-member ring have the same height and form "zigzag" chains along the [01$\bar{1}$] direction. However, due to buckling, one of these two atoms (the up-atom) is shifted upward (out of the surface) while the other (the down-atom) is shifted downward (into the surface), as illustrated in Fig. 1. The occupied surface states are mainly localized on the up-atom, while the empty surface states are mainly localized on the down-atom. Consequently, the bonding surface state band π_{VB} derived from the up-atom orbital is filled, while the antibonding surface state band π^*_{CB} derived from the down-atom orbital is empty.

In Fig. 2 we present typical large-scale [(a)–(c)] and high-resolution [(d)–(e)] STM topography images of the clean Ge(111)2 × 1 surface. Large atomically flat terraces up to 10^5 nm^2 can be observed, which are separated from each other by monatomic steps (MASs). It can be observed in Fig. 2(b) that the Ge(111)2 × 1 surface consists of different types of domains with slightly different atomic arrangement.[54] This is related to the threefold rotational symmetry of the surface. The domains are found to be separated by two different types of domain boundaries (DBs) [see Fig. 2(b)]. At the first type of DB, referred to as a type-A DB following the terminology used in Ref. 54, the atomic rows at the opposite sides of the DB are rotated by an angle $\pi/3$. The second type of DB, the so-called antiphase DB or type-B DB (Ref. 54), is formed due to a shift of the π-bonded chain rows in the [2$\bar{1}$1] direction by half a unit cell. We found that most DBs are of type B and that the type A DBs often exhibit (local) disorder.[55]

In addition, two types of MASs can be observed [see Figs. 2(a) and 2(c)]. With respect to the upper terrace one type of MAS, hereafter referred to as type A, is oblique to the π-bonded chain rows on the terrace. The second type of MAS, hereafter referred to as type B, is parallel to the π-bonded chain rows. One should note that Fig. 2(a) exhibits pronounced Moiré fringes that run along one direction and

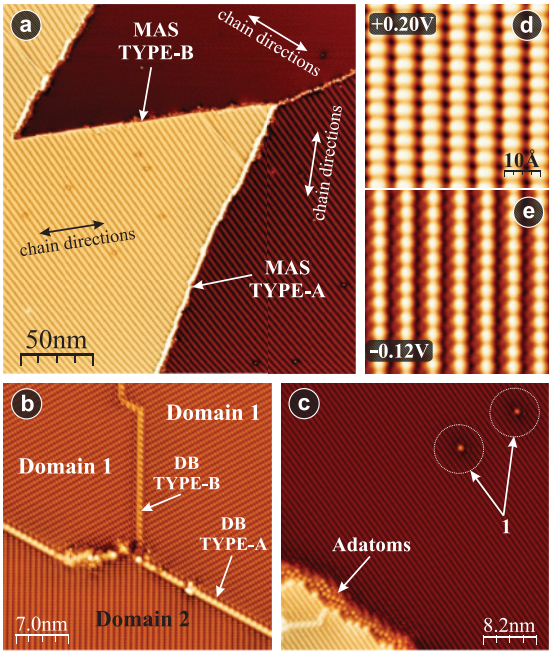

FIG. 2. (Color online) (a)–(c) Typical large-scale STM topography images of the freshly cleaved Ge(111)2 × 1 surface (V_t = +1.0 V, I_t = 35 pA). High-resolution (d) empty and (e) filled state STM images of the same area, recorded at the indicated tunneling voltage V_t and at I_t = 0.9 nA and 3.0 nA, respectively.

become visible because of the large size of the image,[56] while the π-bonded chain rows are not visible on the STM image and their direction is specified by arrows for each of the terraces. We find that Ge adatoms are often present at the MASs, both on the upper and on the lower terrace, except on the upper terrace of type-A MASs. At these terraces the surface is either locally distorted or a 2 × 4 or c2 × 8 surface reconstruction occurs [Fig. 2(c)].[52] The Ge surface adatoms are probably created upon cleavage at room temperature, after which the adatoms can migrate along π-bonded chain rows to the MAS regions. Furthermore, (individual) Ge adatoms can be frequently observed on atomically flat Ge(111)2 × 1 terraces as well above a charged subsurface Ga impurity [see label 1 in Fig. 2(c)]. These adatoms are well separated from each other and their number is in good agreement with the low doping level of our Ge samples.

In Fig. 3 we present a typical normalized conductance spectrum recorded at the p-type Ge(111)2 × 1 surface. The main energy bands are indicated by gray rectangles at the bottom of Fig. 3. In the spectrum the large peak around 0.19 eV can be assigned to the onset of the unoccupied surface state conduction band π^*_{CB} related to the upper π-bonded chains of the Ge(111)2 × 1 surface (see Fig. 1).[57,58] Two energy gaps can be discerned: a narrow gap of about 0.19 eV and a wide gap of about 0.74 eV. The latter corresponds to the forbidden energy gap of the projected bulk band structure of the Ge(111) surface at low temperature. On the other hand, the narrow gap corresponds to the energy gap between the filled bulk valence band (VB) and the unoccupied surface state conduction band (π^*_{CB}). Using STS[53] as well as photoemission experiments,[59–61] the surface state band gap has been determined before, yielding a gap value of 0.54 ± 0.04 eV. From Fig. 3 it can be concluded

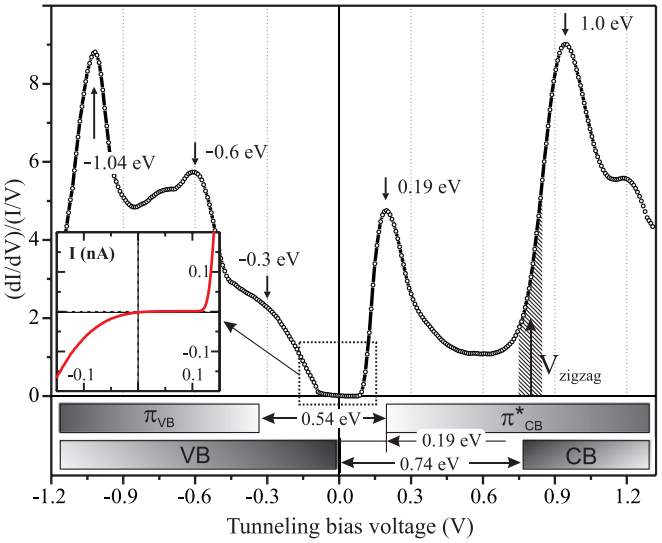

FIG. 3. (Color online) Normalized conductance spectrum recorded on a defect-free area of the freshly cleaved Ge(111)2 × 1 surface. The main energy bands are indicated by gray rectangles at the bottom of the figure (see text for more details). Inset: Current-voltage (I-V) characteristic close to the Fermi energy E_F.

that the high-resolution STM images in Fig. 2(e) and Fig. 2(d) were obtained at tunneling voltages near the top of the VB and the bottom of π^*_{CB}, respectively.

B. Adsorption of Co atoms on Ge(111)2 × 1

In Figs. 4(a) and 4(b) we present two typical large-scale STM topography images of the Ge(111)2 × 1 surface after Co atom deposition corresponding to a coverage of 0.032 MLs. Three different kinds of structures are formed after Co deposition: (i) Co/Ge intermixing layers (ILs) [indicated by the two arrows with label 1 in Fig. 4(a)], (ii) Co clusters consisting of multiple Co atoms [indicated by the two arrows with label 2 in Fig. 4(b)], and (iii) well-separated individual Co atoms [indicated by the two arrows with label 3 in Fig. 4(b)].

The Co/Ge ILs are formed due to the consecutive accumulation of Co atoms at surface/subsurface defects, e.g., DBs and MASs.[62] As indicated by the results of our DFT calculations that are presented below, Co atoms are able to migrate along the π-bonded chain rows, despite the low temperature of the sample during Co deposition ($T_s \leqslant 80$ K). Co/Ge ILs are found both on the upper and lower terraces at type-A MASs. At the type-B MASs, formation of a Co/Ge IL occurs only on the lower terrace. Near DBs Co/Ge ILs are observed on both sides of the type-A and type-B DBs. Co/Ge ILs can be found on atomically flat terraces as well, far away from any DBs and MASs. Since Co-free atomic-size defects, including in particular Ga subsurface impurities,[55] can no longer be observed after Co deposition, this suggest that these defects act as nucleation centers for the formation of Co/Ge ILs. The number of Co/Ge ILs formed on atomically flat terraces roughly scales with the number of atomic-scale defects that is observed prior Co deposition. A more detailed discussion on the formation of Co/Ge ILs will be presented elsewhere.[62]

Only a small fraction of the Co atoms coagulates into small Co clusters. A larger fraction of the Co atoms remains

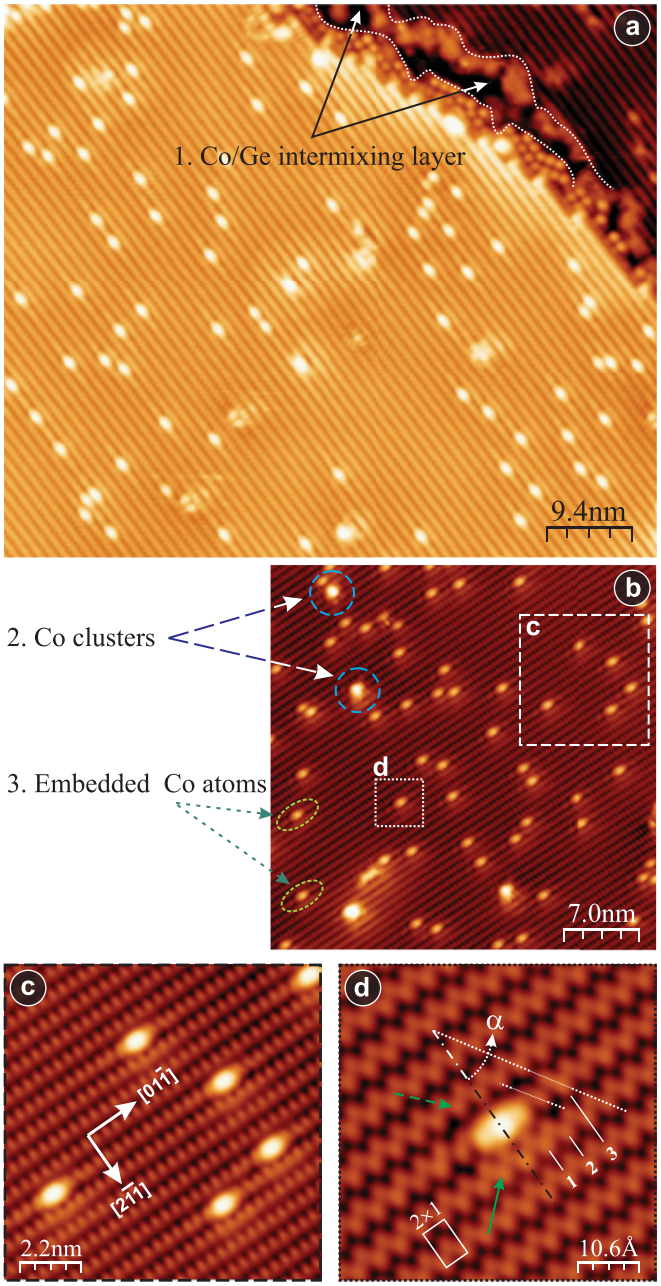

FIG. 4. (Color online) (a), (b) STM topography images of the Ge(111)2 × 1 surface after deposition of 0.032 ML of Co (V_t = +1.0 V, I_t = 15 pA). (c), (d) High-resolution STM images of the areas confined by the dashed rectangle and by the dotted rectangle in (b), respectively [V_t = +0.9 V, I_t = 10 pA for (c) and V_t = +0.80 V, I_t = 300 pA for (d)].

under the form of individual atoms after deposition. At tunneling voltages above 0.7 V these individual atoms appear as bright protrusions located on the upper π-bonded chain rows. At other tunneling voltages the Co atoms are observed differently. This voltage dependence is discussed in more detail in Sec. III C below. High-resolution STM topography images of individual Co atoms are presented in Figs. 4(c) and 4(d). The number of individual Co atoms that can be inferred from Figs. 4(a) and 4(b) is 0.005 ± 0.002 ML. 13 ± 5 % of the deposited number of Co atoms are observed as individual Co atoms, while 87 ± 5 % contribute to the formation of Co/Ge ILs and Co clusters. It is important to already note here that the individual Co atoms are actually not on top of the Ge surface, as will be demonstrated in detail in Sec. IV below by comparing the experimental STM images to simulated STM images based on DFT calculations. According to the DFT calculations, individual Co atoms penetrate into the Ge surface and reside in between the third and the fourth atomic layer (AL), in a quasistable position (at low temperatures) inside the 7-member Ge ring of the 2 × 1 reconstruction (see Fig. 1). This "embedding" is found to influence the local electronic structure but does not give rise to a modified surface reconstruction, as can be seen in Figs. 4(c) and 4(d). We therefore refer to this embedding as "noninvasive."

The low temperature of the Ge substrate during Co deposition appears to be crucial for obtaining individual, well-separated Co atoms. As mentioned above, in spite of the low substrate temperature, the larger fraction (around 87%) of the Co atoms still exhibit sufficient surface mobility to migrate to defects where Co/Ge ILs are formed [see Fig. 4(a)]. The residual fraction of deposited Co atoms (around 13%) remain confined to defect-free atomically flat terraces of the 2 × 1 surface. Recently, we reported that these Co atoms diffuse from their quasistable sites to surface and subsurface defects as well after warming up the sample to room temperature.[62] However, as long as the sample remains at low temperatures, the embedded individual Co atoms remain immobile during the experiments in the investigated −1.5 to + 1.5 V voltage range.

As illustrated in Fig. 4(d), the "zigzag" structure of the 2 × 1 reconstruction of the low-doped p-type Ge(111) surface (see Fig. 1) becomes observable for a limited range of tunneling voltages $V_{zigzag} = 0.85 \pm 0.07$ V. From Fig. 3 we can conclude that both the unoccupied surface states π^*_{CB} (wave functions that are mainly localized on the down-atoms) and the unoccupied states at the bottom of conduction band (CB) (wave functions which are partially localized on the up-atoms[63]) become available for tunneling within this voltage range. Although the wave functions on the up-atoms have a smaller amplitude, the higher position of these atoms implies that they appear more prominently in the STM images than the down-atoms when the applied tunneling voltage increases. Within the V_{zigzag} voltage range (this range is marked by the gray dashed area in Fig. 3), the contribution of π^*_{CB} to the tunneling current remains nearly constant, while the contribution from CB rapidly increases with increasing V_t up to 1.0 V. Hence, a balance exists between tunneling into up- and down-atoms within the V_{zigzag} voltage range, which implies that both the up- and down-atoms of the π-bonded chain rows are visualized in constant-current STM images [see Fig. 4(d)]. We found that the precise value of V_{zigzag} depends on the doping level as well as on the semiconductor type. For example, the 2 × 1 reconstruction of the (111) surface of heavily doped n-type Ge(111) (phosphorus doping level $n_P = 1 \times 10^{19}$ cm^{-3}) reveals zigzag chains around 0.55 V. Previously, it was reported by Trapmann *et al.* that zigzag chains appear around 0.8 V for n-type Si(111)2 × 1 surfaces.[64] The precise value of V_{zigzag} is therefore a characteristic feature of the semiconductor surface under investigation.

From Figs. 4(a)–4(d) it becomes clear that all individual Co atoms occupy identical positions at the Ge surface: Their

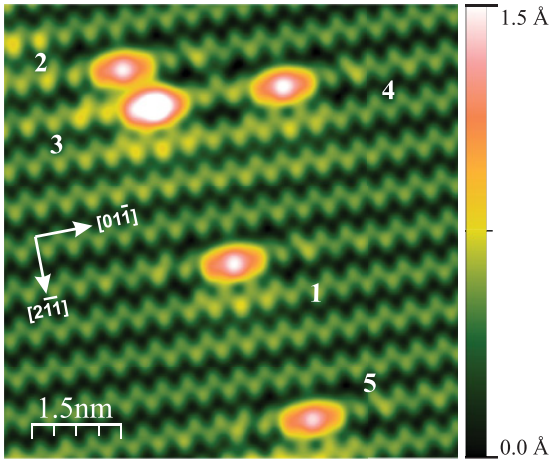

FIG. 5. (Color online) High-resolution STM topography image of 5 Co atoms embedded in the Ge(111)2 × 1 surface ($V_t = +0.8$ V, $I_t = 200$ pA).

appearance is symmetric with respect to the [2$\bar{1}\bar{1}$] direction [the symmetry axis is drawn as a black dash-dotted line in Fig. 4(d)], while they appear asymmetric with respect to the [01$\bar{1}$] direction. The latter can be related to the asymmetry of the 2 × 1 surface reconstruction (due to buckling) along this direction. The relevant crystallographic directions are indicated in Fig. 4(c) and are the same for Figs. 4(b) and 4(d). The symmetry and asymmetry of the Co atoms with respect to the [2$\bar{1}\bar{1}$] and [01$\bar{1}$] directions, respectively, become most clearly resolved for tunneling voltages near V_{zigzag} [see Fig. 4(d) and Fig. 5]. The bright protrusion related to an individual Co atom occupies about 2 surface unit cells along the π-bonded chain rows. Moreover, in Fig. 4(d), disturbance of the zigzag atomic structure along the [01$\bar{1}$] direction can be observed near the Co atom over a distance $\leqslant 3$ unit cell periods. In Fig. 4(d) the edge of the unperturbed zigzag π-bonded chain on the right-hand side of the Co atom is marked by a long dotted white line, forming an angle $\alpha \approx 35^\circ$ with the [2$\bar{1}\bar{1}$] symmetry axis. Closer to the Co atom related protrusion, a brighter and higher feature [marked by the short dotted white line and indicated by the label 2 in Fig. 4(d)] is visible, also making an angle close to α with the [2$\bar{1}\bar{1}$] symmetry axis. The same disturbance is observed to the left of the Co atom (mirror symmetry with respect to the [2$\bar{1}\bar{1}$] direction). Identical characteristic features are observed for all investigated individual Co atoms on differently oriented Ge(111)2 × 1 domains.

In addition to the disturbance of the zigzag structure, an asymmetry of the electronic structure of the neighboring π-bonded chain rows (with respect to the [01$\bar{1}$] direction) near an embedded Co atom is observed. This asymmetry is most clearly resolved in maps of the local density of states (LDOS) (not shown here). It can be observed as well in STM topography images around V_{zigzag}: The lower π-bonded chain row in Fig. 4(d) (indicated by the green solid arrow) appears brighter when compared to subsequent rows, while the upper π-bonded chain row (indicated by the green dashed arrow) does not appear to be influenced by the embedded Co atom. This asymmetric perturbation and the disturbance of the zigzag structure of the π-bonded chain rows always occur simultaneously and were observed with various STM tips. Figure 5 presents an STM topography image of 5 embedded single Co atoms that all induce a similar difference between the Co neighbor chains. As we will demonstrate below when discussing the results of our DFT calculations, this additional asymmetry of the Ge(111)2 × 1 surface induced by the Co atoms allows us to determine the crystallographic [2$\bar{1}\bar{1}$] direction of the different Ge(111)2 × 1 domains, leading to the conclusion that all investigated Ge(111)2 × 1 surfaces consist of domains with π-bonded chain-left isomers (negative buckling) exclusively.

There appears no significant electronic interaction between two embedded single Co atoms that reside in the same π-bonded chain row in close vicinity (down to a distance of 3 unit cells along the [01$\bar{1}$] direction) in the investigated voltage range from −1.5 to +1.5 V [see Figs. 4(a) and 4(b), as well as Co atoms (3) and (4) in Fig. 5]. On the other hand, an electronic interaction effect can be observed for Co atoms that reside in neighboring π-bonded chain rows at a distance (in the π-bonded chain row direction) smaller than ±3 unit cells. This is illustrated in Fig. 5. Indeed, the lower Co atom (3), which is located on a π-bonded chain row that is perturbed by the upper Co atom (2), exhibits modified electronic properties. More precisely, Co atom (3) appears brighter in Fig. 5, while Co atom (2) appears similar to the other Co atoms. Note that the modified electronic properties of Co atom (3) are caused by Co atom (2) only and are not related to the presence of the neighboring Co atom (4) that is located in the same π-bonded chain row.

C. Voltage-dependent STM investigation of single Co atoms embedded in Ge(111)2 × 1

In this section we focus on the novel Co-induced electronic features by careful comparison to the electronic properties of the clean Ge(111)2 × 1 surface (see Sec. III A). First of all it must be noted that deposition of (a small number of) Co atoms does not change the electronic properties of the defect-free Ge(111)2 × 1 surface: The characteristic peaks in the STS spectra of the clean Ge(111) surface prior to Co deposition (Fig. 3) are still observed at the 2 × 1 reconstructed surface after Co deposition. Figure 6 presents a series of (a) empty and (b) filled state STM topography images of 3 individual, well-separated Co atoms embedded in the reconstructed Ge(111)2 × 1 surface. Images are recorded at the same location and with the same tip for a broad range of tunneling voltages V_t between 1.4 V and −1.5 V. The series of images reveals a pronounced voltage dependence for both the clean p-Ge(111)2 × 1 surface and the electronic influence of the embedded Co atoms on the π-bonded chain rows.

In the empty-state regime, at high voltages above 1.0 V [Figs. 6(a5) and 6(a6)], topography is dominated by the reconstruction lines of the π-bonded chain rows in the [01$\bar{1}$] direction. Individual Co atoms appear as bright protrusions, located directly on the upper π-bonded chain row and extending over 2 unit cells of the 2 × 1 reconstruction. Maximum contrast of the Co-related features is observed around $V_t = 0.93$ V and above this voltage the contrast again decreases. This is because the contribution of the π^*_{CB} surface states to the tunneling current remains approximately constant, while the

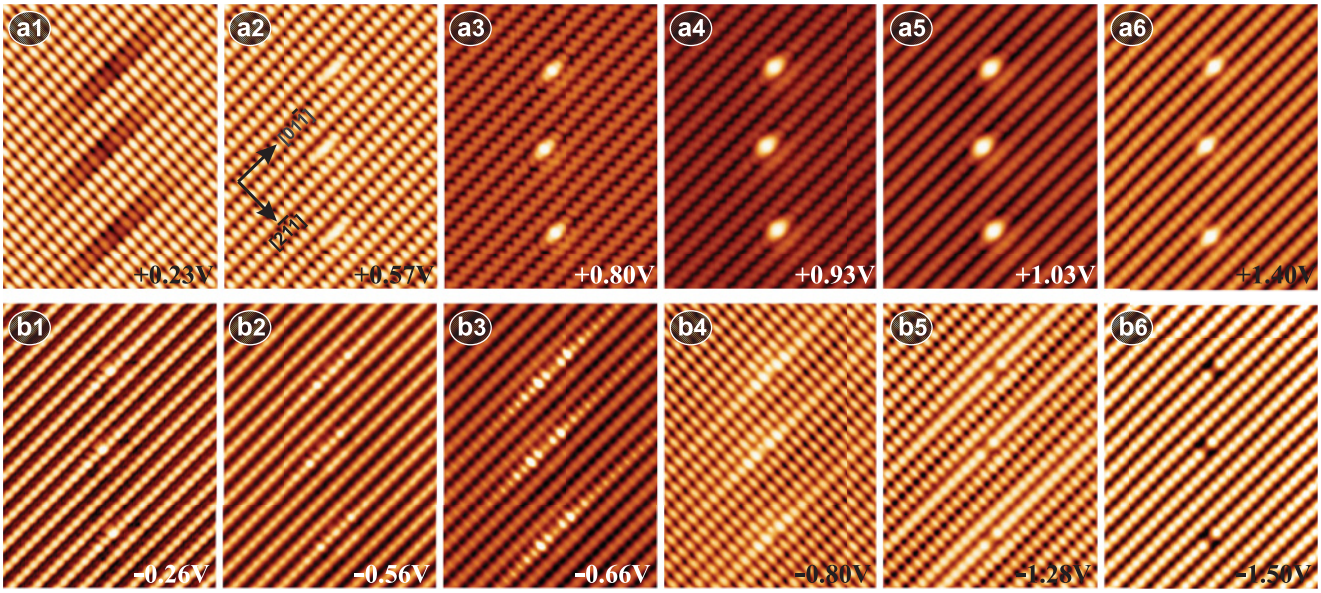

FIG. 6. (Color online) (a1)–(a6) Empty-state and (b1)–(b6) filled-state STM topography images of 3 single Co atoms embedded in the Ge(111)2 × 1 surface. Image sizes are 15.0 × 11.2 nm^2. The tunneling voltage V_t is indicated for each image. Tunneling current I_t is 180 pA, 300 pA, 320 pA, 340 pA, 340 pA, and 340 pA for (a1), (b1) to (a6), (b6), respectively.

contribution of the bulk CB states increases with increasing tunneling voltage (see Fig. 3). At lower voltages around $V_{\text{zigzag}} = 0.80$ V [Fig. 6(a3)] the zigzag atomic structure discussed above emerges. Around $V_t = 0.60$ V contrast of the Ge atomic corrugation and the Co-related protrusions becomes similar and Co atoms can mainly be discerned by the locally induced perturbation of the 2 × 1 surface reconstruction [Fig. 6(a2)]. In the empty-state regime below 0.60 V [Figs. 6(a1) and 6(a2)] extra corrugation appears in the STM topography along the [2$\bar{1}\bar{1}$] direction. Close to the Fermi level E_F the strength of this extra corrugation along the [2$\bar{1}\bar{1}$] direction becomes comparable to the corrugation along the [01$\bar{1}$] direction [Fig. 6(a1); also see Fig. 2(d)]. Co atoms appear as centrosymmetric striped depressions along the π-bonded chain rows. These depressions exhibit a local minimum directly above the embedded Co atom and gradually fade away with increasing distance (up to 4 nm) from the local minimum [Fig. 6(a1)].

In the filled-state regime, at voltages close to E_F, topography is again dominated by corrugation of the π-bonded chain rows [Fig. 6(b1); also see Fig. 2(e)]. Maxima of the atomic corrugation are related to the highest filled bulk VB states that are localized on the Ge up-atoms (see Fig. 1). Co atoms appear as bright protrusions located on the π-bonded chain rows [Fig. 6(b1)]. Below −0.7 V extra corrugation emerges along the [2$\bar{1}\bar{1}$] direction [Fig. 6(b4)] and persists down to around −1.2 V. Below −1.2 V topography becomes again completely dominated by the π-bonded chain rows along the [01$\bar{1}$] direction [Fig. 6(b6)]. Here, Co atoms appear as atomic-size vacancies in the upper π-bonded chain rows of the 2 × 1 surface reconstruction [Figs. 6(b5) and 6(b6)].

It is clear from Figs. 6(a1) and 6(b2)–6(b5) that the embedded Co atom induces a localized 1D perturbation of the LDOS along the π-bonded chain rows. STM images recorded with a tunneling voltage near the edge of the surface-state bands reveal highly anisotropic scattering of electrons and screening effects with 1D confinement to the π-bonded chains. 1D perturbations have previously been reported for Si(111)2 × 1[64–66] and Ge(111)2 × 1[55] surfaces. Here, the perturbation near the atomic-size defect has a pronounced 1D shape[64] and extends up to 6 nm along the π-bonded chain rows, while the width of the perturbation remains limited to one period (0.69 nm) of the 2 × 1 reconstruction in the [2$\bar{1}\bar{1}$] direction. In the empty-state regime, the 1D screening effects appear as depressions and become most pronounced near 0.23 eV, corresponding to the bottom of the surface-state band π^*_{CB} [Fig. 6(a1)]. In the filled-state regime, the 1D electron scattering effects are observed as protrusions and are most clearly seen near −0.66 V, corresponding to the top of the surface-state band π_{VB} [Fig. 6(b3)]. In both regimes the 1D perturbations exhibit identical mirror-like symmetry with respect to the [2$\bar{1}\bar{1}$] direction, similar to our recent observations for atomic-size surface impurities on Ge(111).[55]

In summary, we can state that individual Co atoms embedded in Ge(111)2 × 1 surfaces exhibit the following general properties:

(1) Individual Co atoms penetrate into the cold ($T_s \leqslant 80$ K) Ge(111)2 × 1 surface after deposition (see Sec. IV below for more details);

(2) the 2 × 1 reconstruction is preserved after the noninvasive embedding of a Co atom;

(3) the embedded Co atoms occupy identical positions in the Ge(111) surface and exhibit an identical voltage dependence of the STM topography images;

(4) the embedded Co atoms exhibit a clear symmetry with respect to the [2$\bar{1}\bar{1}$] direction, while they exhibit a clear asymmetry with respect to the [01$\bar{1}$] direction;

(5) the embedded Co atoms induce highly anisotropic scattering of electrons, which is accompanied by screening effects with 1D confinement along the π-bonded chain rows.

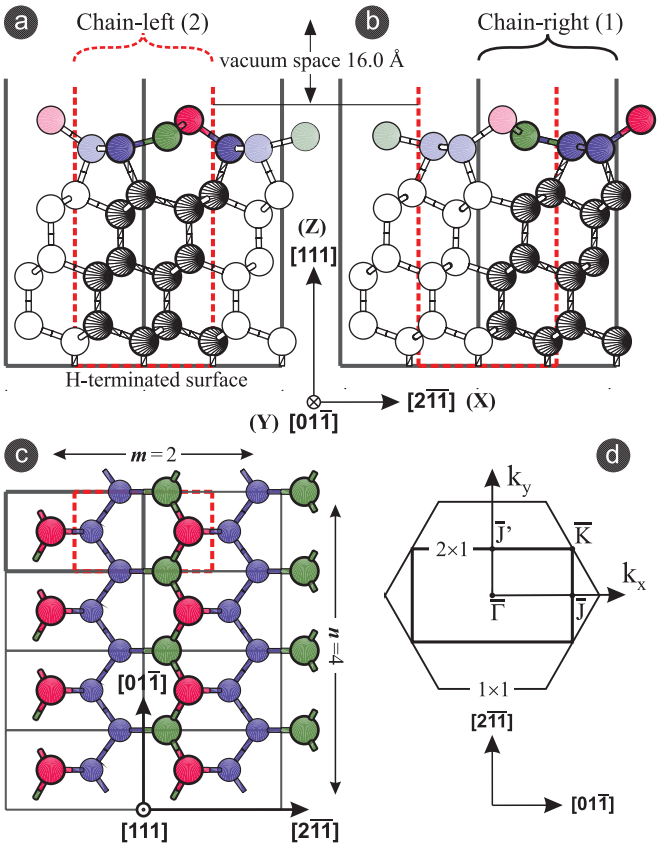

FIG. 7. (Color online) The final position of the 9 topmost Ge layers of the Ge(111)2 × 1 surface reconstruction. (a) Chain-left and (b) chain-right isomers of the Pandey π-bonded chain model with buckling (side view). (c) Top 3 surface atomic layers of the 4 × 2 SC chain-left Ge(111)2 × 1 isomer model (top view). (d) Surface Brillouin zone and relevant directions of the Ge(111)2 × 1 surface.

IV. DISCUSSION AND COMPARISON WITH DFT CALCULATIONS

A. DFT model of the Ge(111)2 × 1 surface

The 2 × 1 reconstruction of cleaved Si and Ge (111) surfaces[52,67–70] is well described by the commonly used Pandey π-bonded chain model described above.[51] The Pandey chain geometry leads to a strong coupling of the dangling-bond orbitals along the chain, while the coupling between the chains is much weaker. This geometry does not take into account the effects of buckling, so that the two uppermost surface Ge atoms in the 7-member rings are at the same height.[51] Northrup *et al*. predicted buckling of the two uppermost atoms by about 0.8 Å (see Fig. 1).[50] This buckling further reduces the surface energy of the system, yielding two different isomers commonly referred to as π-bonded "chain-left" and "chain-right" isomers[71] (see Fig. 7). Relying on first-principles calculations within the computational accuracy that could be achieved at that time (1991), it was found that the chain-left isomer is 6 meV per 1 × 1 surface cell lower in energy when compared to the chain-right isomer. It has been confirmed theoretically[72] and experimentally[63,73] that the chain-left isomer is indeed the dominant isomer at the Ge(111)2 × 1 surface. However, because of the very small energy difference between the two different isomers, coexistence of both surface reconstructions and hence the possible existence of Ge(111)2 × 1 multidomain surfaces cannot be totally excluded.

Our theoretical investigation of the noninvasive embedding of Co atoms in the Ge(111)2 × 1 surface was performed based on DFT[74] within the local density approximation (LDA).[75] Calculations were performed with the SIESTA package,[76–78] which relies on the expansion of the Kohn-Sham orbitals by linear combination of pseudoatomic orbitals. In all calculations a double-zeta basis set with polarization was used. The core electrons were implicitly treated by using norm-conserving Trouiller-Martins pseudopotentials[79] with the following electronic configuration of the elements: H $1s^1$, Ge (Ar $3d^{10}$) $4s^2\,4p^2$, and Co (Ar) $4s^2\,3d^7$, where the core configurations are indicated between parentheses. A cutoff energy of 200 Ry was introduced for the grid integration, ensuring convergence of the total energy of the system within typically 0.1 meV.

Our calculations are performed in three stages. First, we determine the surface equilibrium geometry for the chain-left and chain-right isomers within one surface unit cell (SUC) using conjugate gradient (CG) geometry optimization. Second, based on the Ge(111)2 × 1 SUC, a new $n \times m$ supercell (SC) with one Co atom above the surface is constructed and the equilibrium configurations of Co/Ge(111)2 × 1 are determined relying on CG geometry optimization. Third, the electronic structure of a still larger SC is calculated, which is then used to perform the DFT-based STM topography image simulations.

In order to model the Ge(111)2 × 1 surface, a reduced square SUC (unreconstructed) with $(a_0\sqrt{2}, a_0\sqrt{6})$ lattice vectors is used ($a_0 = 2.8205$ Å is half the optimized bulk Ge lattice constant). This SUC consists of a slab of 26 Ge atomic layers, of which one atomic layer is saturated by hydrogen atoms (52 Ge atoms and 2 H atoms per SUC). In the CG geometry optimization the 14 topmost atomic Ge layers are allowed to move, while the 12 layers of Ge and H atoms are frozen at the ideal (bulk) positions. Using 130 $\boldsymbol{k}$ points within the surface Brillouin zone, the atoms are relaxed until all atomic forces acting on the released atoms are smaller than 3 meV/Å, and the remaining numerical error in the total energy is smaller than 0.1 meV for each optimization step.

The final positions of the 9 topmost Ge layers yielding the Ge(111)2 × 1 surface reconstruction are presented in Figs. 7(a) and 7(c) (chain-left isomers) and Fig. 7(b) (chain-right isomers). The coordinates of the Ge atoms below the seventh atomic layer are found to change only slightly during the CG geometry optimization. For the considered SUC the two different Ge isomers are both possible for the formation of the 2 × 1 reconstruction. Depending on the initial conditions, either the 5-member or the 7-member Ge ring of the reconstruction is present in the 2 × 1 SUC. This is illustrated in Figs. 7(a) and 7(c) for the chain-left isomer. The black solid bars in Figs. 7(a) and 7(c) comprise the 5-member ring SUC, while the red dashed bars comprise the 7-member ring SUC. The same can be done for the chain-right isomer, as illustrated in Fig. 7(b). For the 5-member ring the upper π-bonded chain rows are formed at the joint of the SUC in the [2$\bar{1}\bar{1}$] direction and are referred to as "chain-left/right (1)" hereafter [see, e.g., the solid colored atoms in Fig. 7(b)]. For the 7-member ring, the upper π-bonded chain rows are formed inside the SUC and are referred to as "chain-left/right (2)" hereafter [see, e.g., the solid colored atoms in Fig. 7(a)]. We verified

that the chain-left/right (1) and chain-left/right (2) selections exhibit identical electronic properties for periodical boundary conditions. Depending on the position of the adsorbed Co atom with respect to the upper π-bonded chain rows in the $n \times m$ SC, selection (1) or (2) was chosen. Buckling distances of the chain-left and chain-right isomers are 0.83 Å and 0.80 Å, respectively. The chain-right isomer has a total surface energy that is 14 meV/(2 × 1 SUC) higher than the total surface energy of the chain-left isomer, implying that the chain-left isomer should be the dominant isomer for the Ge(111)2 × 1 surface.[63,72,73]

B. Co adsorption sites and energy decomposition

To model the adsorption of a Co atom on the Ge(111)2 × 1 surface, we used the 9 topmost relaxed Ge layers for the chain-left and the chain-right isomer that were obtained following the procedure described above (also see Fig. 7). 6 of these 9 atomic layers are allowed to relax. The bottom side of the 3 fixed atomic layers is saturated by hydrogen atoms (16 Ge atoms and 2 H atoms per SUC; 16 Å slab vacuum space separation).

Geometry optimization was carried out for an enlarged 4 × 2 SC for both the chain-left and the chain-right isomers. In Fig. 7(c) we show the three topmost layers of the 4 × 2 SC (size is 15.95 × 13.81 Å, consisting of 145 atoms) for the chain-left (1) isomer geometry. A Co atom was then located in front of the Ge(111)2 × 1 surface. Next, the relaxation of the Co atom was calculated by means of CG geometry optimization. CG geometry optimization for the 4 × 2 SC was carried out until all atomic forces acting on the released Co and Ge atoms were below 5 meV/Å and until the numerical error on the total energy was smaller than 10^{-4} eV per SC for each optimization step. Using a variety of starting coordinates for the Co atom, multiple Co/Ge quasistable geometries were tested and their total energies were compared. Both chain-left and chain-right isomer geometries were used. In both cases multiple quasistable Co atom sites (with respect to an atomic force tolerance 5 meV/Å) were found, including sites on the Ge(111)2 × 1 surface as well as underneath the Ge(111)2 × 1 surface, i.e., inside the big 7-member Ge ring. The subsurface sites were identified by using a location inside the 7-member ring as the starting location for the CG geometry optimization. On the other hand, the surface sites were identified by using an initial Co location above the Ge(111)2 × 1 surface, at heights in the 3 to 4 Å range and at various initial coordinates in the (x, y) plane. 23 different positions were used in total for the starting position of the Co atom in the SUC for the chain-left isomer geometry, of which 18 are located on the Ge(111)2 × 1 surface and 5 underneath the Ge(111)2 × 1 surface. From all these positions, 9 quasistable sites were identified for the chain-left isomer, of which 6 are located on the Ge surface and 3 are located inside the 7-member ring underneath the Ge surface. The other starting positions were found to develop in one of these 9 quasistable positions during the CG geometry optimization process within the 4 × 2 SC. For the chain-right isomer we found 8 quasistable sites, of which 5 are located on the Ge(111)2 × 1 surface and 3 underneath the Ge(111)2 × 1 surface.

In Table I we present for the chain-left isomer geometry and for all possible quasistable Co atom sites [labeled (1) to (9) in the first column] an overview of the calculated difference ΔE_{sites} in total energy with respect to the total energy for the Co atom located at site (7). For a 4 × 2 SC size (second column) the minimum energy was found to occur for the Co atom located at site (7). For 3D plots visualizing the calculated quasistable geometries of the Co sites listed in Table I we refer the reader to the next section as well as to the Appendix. Similar calculations were performed for the chain-right isomer geometry and for a 4 × 2 SC (data not shown). Again, the minimum energy was found for the case of a Co atom located inside the 7-member ring, but with somewhat lower energy gain when compared to the chain-left geometry.

TABLE I. Calculated difference ΔE_{sites} in total energy for the Co atom located at the different sites (on top [(1)–(6)] and underneath [(7)–(9)] the Ge(111)2 × 1 surface) and the Co atom located at site (7). The calculated energy differences are for the chain-left isomer geometry and are given for 4 × 2, 8 × 4, and 14 × 4 SCs. Values are in units of eV.

Co Site Number	4 × 2 SC	8 × 4 SC	14 × 4 SC
(1)	1.791	moves to site (2)	
(2)	0.376	0.724	1.250
(3)	0.583	0.730	0.841
(4)	0.966	1.199	1.350
(5)	2.280	2.470	
(6)	0.701	1.054	1.280
(7)	0	0	0
(8)	0.038	0.129	0.462
(9)	0.512	0.595	0.693

In order to reduce the influence (related to the periodic boundary conditions) of the restructuring induced by the Co atom within a 4 × 2 SC, similar calculations were performed for a 8 × 4 SC (size is 31.90 × 27.63 Å, consisting of 577 atoms). The obtained values for the difference ΔE_{sites} in total energy for all possible quasistable Co atom sites after CG geometry optimization are listed in the third column of Table I. Similar to the case of the 4 × 2 SC, the energy difference is again with respect to the total energy for the Co atom at site (7). When using this larger SC, a transition of the Co atom was found from site (1) to site (2). Also, site (9) was found to be energetically more favorable than site (2) when compared to the 4 × 2 SC. This can be explained by the occurrence of longer range surface relaxations inside the larger SC. Remarkably, for the 8 × 4 and 14 × 4 SCs all Co sites inside the 7-member ring have a lower energy (see Table I) with respect to the other sites, which is different from the 4 × 2 SC.

Finally, calculated energy values for a 14 × 4 SC (size is 55.82 × 27.63 Å, consisting of 1009 atoms) are presented for the chain-left isomer geometry in the fourth column of Table I. Similar calculations were performed for the chain-right isomer geometry (data not shown) and yielded nearly identical results, with again a somewhat lower energy gain with respect to the other sites when compared to the chain-left geometry.

C. Prime location of the Co atom into Ge(111)2 × 1 surface

In Fig. 8(a) we present a 3D ball-and-stick model view of the relaxed Ge(111)2 × 1 surface, obtained for the 8 × 4 SC

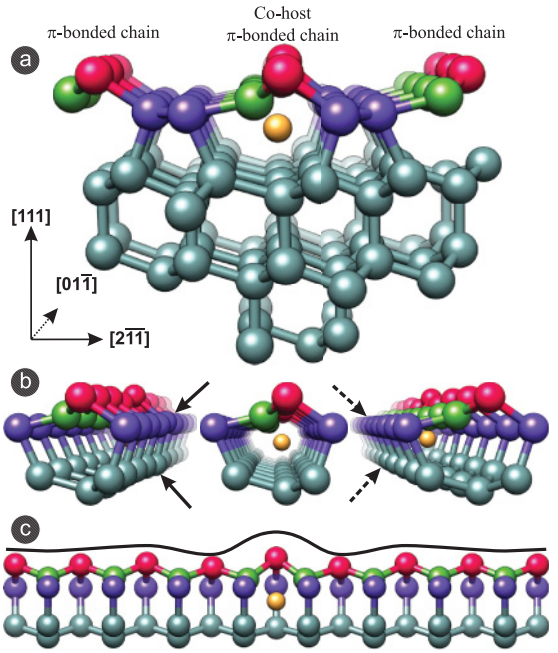

FIG. 8. (Color online) Calculated minimum energy position of a single Co atom (yellow) at the Ge(111)2 × 1 surface. The Co atom is in between the third and fourth atomic layer underneath the Ge surface. (a), (b) 3D view of the chain-left Ge isomer. The Co atom is located inside the 7-member Ge ring (viewed along the [01$\bar{1}$] direction). (c) Side view of the Co-host chain-left isomer (viewed along the [2$\bar{1}\bar{1}$] direction). Height variations of the up-atoms in the π-bonded chain row are indicated by the black envelope curve (magnified by a factor 2 for clarity).

with chain-left isomer geometry. The Co atom is located at the site of minimum energy, i.e., site (7) (see third column in Table I). Similar 3D ball-and-stick model views of the calculated quasistable geometries for the other Co sites listed in Table I are presented in Fig. 16 and Fig. 17. A 3D front view and a side view of the Co atom inside the 7-member ring are presented in Fig. 8(b) and in Fig. 8(c), respectively. Relaxation of the surface Ge up-atoms and down-atoms upon Co atom incorporation can be clearly observed. The black solid envelope line in Fig. 8(c) reflects the variation of the z coordinate of the center of the Ge up-atoms (magnified by a factor 2 for clarity). The upward shift of the Ge up-atom located directly above the Co atom is +0.43 Å, while the downward shift of the neighboring Ge up-atoms is −0.10 Å. The Co-induced shift of the z coordinate of the Ge up- and down-atoms extends as far as ±3 periods along the π-bonded chain row of the 2 × 1 reconstruction, in agreement with our experimental observations [see Fig. 4(d) and the related discussion in Sec. III B].

The black solid arrows in Fig. 8(b) (left image) indicate the bulk Ge atoms that experienced the most significant shift of their positions upon embedding of the Co atom. In Fig. 8(b) (right image) it can be seen that the Ge atoms to the left of the Co atom (indicated by the black dashed arrows) remain unperturbed. This asymmetry of the geometry (and hence of the local electronic properties) of the Co/Ge(111)2 × 1 system along the [01$\bar{1}$] direction is in agreement with our experimental observations: The STM topography images in Fig. 4(d) and Fig. 5 also exhibit an asymmetry with respect to the [01$\bar{1}$] direction around an embedded Co atom. Finally, we want to stress once more that the embedding of Co atoms does not give rise to a novel Ge surface reconstruction. Instead, the Ge atoms surrounding the Co atoms experience only small changes of their positions, which is accompanied by changes of the local electronic properties as well. Experimentally, we also found that the 2 × 1 reconstruction is maintained upon Co embedding, as becomes clear in Figs. 6(a1), 6(a2), 6(b1), and 6(b2). Calculations for the other Co atom sites in Table I reveal that these sites lead to more drastic changes and in some cases even local destruction of the Ge(111)2 × 1 reconstruction. It can be seen in Fig. 17 that the Co atom at site (5) induces a significant modification of the 2 × 1 reconstruction, while the Co atoms at sites (6) and (8) locally destroy the 2 × 1 reconstruction of the upper π-bonded chain; i.e., the periodicity of the Ge up- and down-atoms is broken along the [01$\bar{1}$] direction.

D. Embedding of a Co atom into the Ge(111)2 × 1 surface

In this section we will discuss the two most feasible routes for the incorporation or penetration of a Co atom, which is initially above the Ge(111)2 × 1 surface, to the site (7), i.e., inside the 7-member ring of the Ge(111)2 × 1 surface. Embedding of deposited atoms into subsurface layers has already been demonstrated before for a Si[80] surface and for a Ge[81,82] surface. Ge atoms have been found both experimentally and theoretically to penetrate into the fourth subsurface layer of Si(100)[80] when deposited at a substrate temperature of about 500 °C. Similarly, it has been found that Si atoms deposited on Ge(100)2 × 1 are able to move below the Ge surface at room temperature.[81] Finally, the formation of Co/Ge intermixing layers up to 3 MLs thick after deposition of Co atoms on room temperature Ge(111) substrates has been demonstrated experimentally.[83]

As a possible starting site for penetration into the 7-member ring, the energetically two most favorable quasistable Co atom sites on top of the Ge(111)2 × 1 surface are considered: site (2) and site (3) (see Table I). A 3D visualization of both configurations is presented in Fig. 9. The crystallographic directions of Fig. 9 are identical to those of Fig. 8(a) (except for a rotation of the viewpoint angle with respect to the [111] direction). For the sites (2) and (3) the Co atoms are located in between two neighboring upper π-bonded chain rows, at the center of the hexagonal 6-member Ge ring on

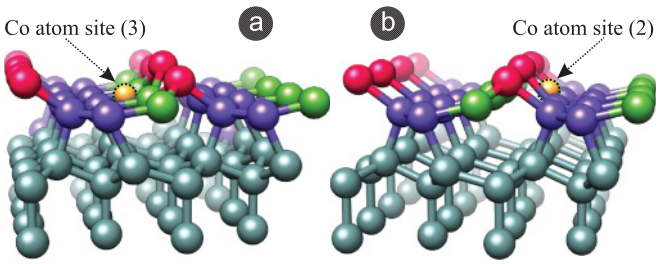

FIG. 9. (Color online) (a), (b) Calculated quasistable geometry (4 × 2 SC) for Co sites (3) and (2) at the Ge(111)2 × 1 surface (see Table I).

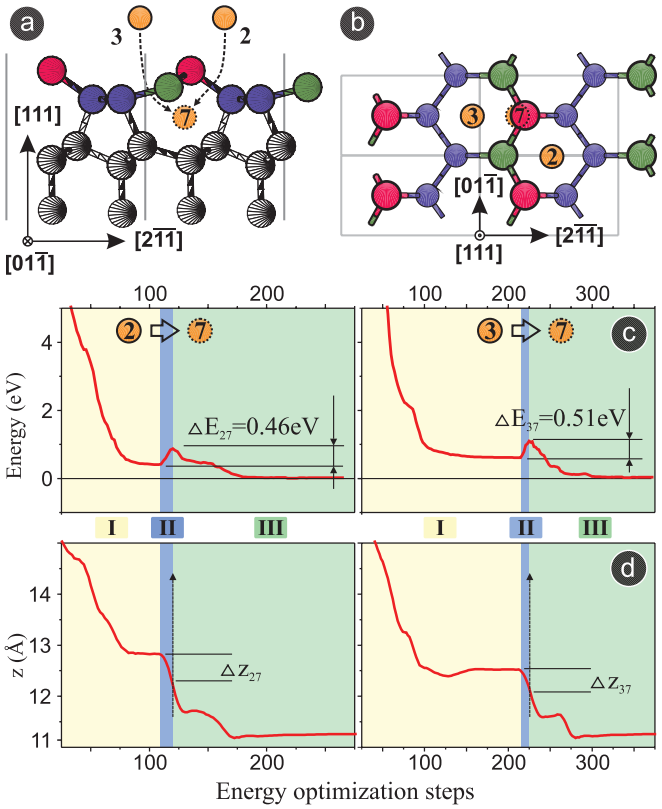

FIG. 10. (Color online) Two different routes are possible for the noninvasive embedding of a Co atom from the vacuum side of the Ge surface into the big 7-member ring of the Ge(111)2 × 1 surface reconstruction [also see Fig. 8(a)]: from position (2) to (7) and from position (3) to (7). (a) Side and (b) top view of the chain-left isomer of the Ge(111)2 × 1 surface reconstruction. (c) Relative changes of the total energy of the Ge(111)2 × 1 4 × 2 SC (including the Co atom) during subsequent geometry relaxation steps for both routes. (d) Corresponding variation of the z coordinate of the Co atom.

the left-hand [Fig. 9(a)] and right-hand side [Fig. 9(b)] of the central upper π-bonded chain row. A top view of these sites at the Ge(111)2 × 1 surface is presented in Fig. 10(b). The Co atom at site (2) has one neighboring Ge down-atom and two neighboring Ge up-atoms, while the Co atom at site (3) has one neighboring Ge up-atom and two neighboring Ge down-atoms. One should note that for both sites the Co atom is already somewhat below the first Ge layer, having a z coordinate comparable to that of the down-atom for site (2) and 0.1 Å lower than the down-atom for the site (3). As was the case for site (7), these Co atom sites do not destroy the reconstruction of the Ge(111)2 × 1 surface.

Next, both quasistable Co positions were taken as the starting positions for additional first-principles DFT calculations with a 4 × 2 SC and using the same parameters as described above. The Co atom was forced to "move" into the bulk of the Ge by sequential decrements of its z coordinate ($\Delta z = 0.04$ Å for each geometry relaxation step). After each forced sequential decrement of the z coordinate, the position of the Co atom is kept fixed, while the Ge atoms are allowed to relax and the total energy is determined. By monitoring the total energy of the 4 × 2 SC during subsequent geometry relaxation steps, we are able to evaluate the potential barrier height that needs to be overcome by the Co atom when diffusing either from site (2) or from site (3) to site (7) without destroying the 2 × 1 surface reconstruction. First, when the Co atom is forced to move only very slightly below the Ge surface, the Co atom "bounces" back to its initial position. Second, upon a certain minimum translation Δz along the z direction (corresponding to a potential barrier ΔE), the released Co atom continues to move farther below the Ge surface to site (7) [see Figs. 10(a) and 10(b)]. Both Co atom trajectories are visualized schematically in Fig. 10(a).

The variation of the total energy E_{tot} of the 4 × 2 SC [again with respect to E_{tot} of the 4 × 2 SC with the Co atom at site (7)] and the variation of the z coordinate of the Co atom during the subsequent geometry relaxation steps are presented in Fig. 10(c) and in Fig. 10(d) for the two considered routes. Three regimes can be discerned. Regime I describes the energy gain and z-coordinate variations during movement of the Co atom from vacuum to either site (2) or site (3). Regime II corresponds to the "forced movement" of the Co atom into the bulk of the Ge up to the "point of no return" when the potential barrier has been overcome. Finally, regime III reflects the subsequent relaxation of the Co atom toward its final and stable position at site (7) in the 7-member Ge ring. The number of geometry relaxation steps for route (2)⇒(7) and for route (3)⇒(7) is 500 and 700, respectively. For clarity, geometry relaxation intervals where the total energy E_{tot} and the z-value remain almost constant (at the end of the regimes I and III) are cut from Figs. 10(c) and 10(d). The graphs presented in Fig. 10(c) allow us to determine the potential barrier that the Co atom needs to overcome for route (2)⇒(7) [(3)⇒(7)]: $\Delta E_{27} = 0.46$ eV [$\Delta E_{37} = 0.51$ V], corresponding to a change in z-coordinate $\Delta z_{27} = 0.48$ Å [$\Delta z_{37} = 0.40$ Å] in Fig. 10(d).

To overcome the surface potential barrier for penetration below the Ge surface, a Co atom must have a sufficiently high (kinetic) energy upon deposition. In our experiments Co atoms are evaporated using an e-beam evaporator, where the Co material is heated to a high temperature T_{v} around 3000 K.[84,85] Atoms leaving an e-beam melt generally have a narrow energy distribution[86] and the kinetic energy of the evaporated cloud of Co atoms, which is induced by the high-temperature evaporation process, can be roughly estimated using the equipartition theorem, yielding a mean atomic kinetic energy of about 0.38 eV. Recently, however, Asano *et al.* have demonstrated experimentally that the velocity of evaporated atoms is typically even higher than the maximum velocity suggested by the ideal-gas approximation.[84] The increased velocity can be accounted for by a conversion of electron excitation energy to kinetic energy during the adiabatic expansion away from the heated material. If the gas flow of evaporated atoms cooled sufficiently during the adiabatic expansion, the resulting maximum velocity can be estimated as[87]

$$v_{\mathrm{max}} = \sqrt{\frac{2}{m}\frac{\gamma}{\gamma - 1} R\, T_{\mathrm{v}}}, \qquad (1)$$

where γ is the specific-heat ratio $C_{\mathrm{p}}/C_{\mathrm{v}}$ (C_{p} and C_{v} are the specific heat at constant pressure and at constant volume per mole, respectively), R is the gas constant, and m is the molar

mass of the evaporated atom. γ is 5/3 for an ideal monoatomic gas. For $T_v \simeq 3000$ K, Eq. (1) yields a maximum velocity $v_{max} = 1460$ m/s and hence the kinetic energy of the deposited Co atoms may exceed even a maximum value of 0.63 eV. This kinetic energy allows a Co atom to overcome the surface energy barrier $\Delta E_{27} = 0.46$ eV or $\Delta E_{37} = 0.51$ eV that is encountered when penetrating below the Ge(111)2 × 1 surface following the route (2)⇒(7) or the route (3)⇒(7), respectively [see Fig. 10(c)].

E. DFT-based modeling of STM topography images

Our theoretical findings, related to the changes in surface energy and the potential barrier for penetration below the surface, support the idea of a noninvasive embedding of individual Co atoms in subsurface 7-member Ge rings. To verify the proposed "embedding model," we investigated the electronic properties of the Co/Ge(111)2 × 1 system by simulating the corresponding STM topography images using DFT-based calculations for a wide range of voltages, which allows for a direct and detailed comparison between theory and experiment. For this purpose we investigated the electronic structure of the Ge(111)2 × 1 surface for each of the possible Co atom locations described in Sec. IV B, for both chain-left and chain-right isomers. The calculated quasistable geometries of the relaxed 8 × 4 SCs (9 and 8 possible geometries for the chain-left and chain-right isomer, respectively) were transferred to a larger 14 × 4 SC (size is 55.82 × 27.63 Å) for which we calculated the electronic properties in detail.

In order to construct STM constant-current topography images based on the calculated electronic structure of the Co/Ge(111)2 × 1 system, the decay of the electron wave functions from the surface into the vacuum needs to be taken into account. Within the Tersoff-Hamann theory[88,89] the dependence of the tunneling current I on the applied tunneling voltage V_t between an STM tip and a surface is given by

$$I = \frac{2\pi e}{\hbar} \sum_{\mu,v} f(E_\mu)[1 - f(E_v + eV_t)]|M_{\mu v}|^2 \delta(E_\mu - E_v), \tag{2}$$

where $f(E)$ is the Fermi function, $M_{\mu v}$ is the tunneling matrix element between electronic states ψ_μ of the tip and electronic states ψ_v of the surface, and E_μ (E_v) is the energy of the state ψ_μ (ψ_v) in the absence of tunneling. When we assume localized wave functions ψ_μ for the tip, $M_{\mu v}$ will vary proportional to the amplitude of ψ_v at the position $\vec{r}_0$, which corresponds to the center of the sphere that is used to approximate the tip apex. At low temperatures and for small tunneling voltages V_t, Eq. (2) reduces to

$$I \propto \sum_v |\psi_v(\vec{r}_0)|^2 \delta(E_\mu - E_F). \tag{3}$$

From Eq. (3) it follows that the tunneling current I is proportional to the surface LDOS that is probed at position $\vec{r}_0$ of the tip, integrated over an energy range from E_F to $E_F + eV_t$. For constant tunneling current $I = I_t$ the STM tip essentially follows a contour of constant surface LDOS. However, because the surface wave functions decay exponentially into the vacuum region, numerical evaluation of $\psi_v(\vec{r}_0)$ for tip-surface distances of the order of several angstroms becomes a significant problem for DFT calculations.[90] For this reason STM simulations are often restricted to (the vicinity of) the surface, which may yield incorrect results. To tackle this problem, we have used the 2D Fourier transform of the wave functions $\psi_v(\vec{r})$ in combination with spatial extrapolation techniques[91] to evaluate the surface wave function $\psi_v(x,y,z)$ in the vacuum region up to $z = 7$ Å above the surface.

In this way we calculated the STM topography images for all available Co atom sites and for both the chain-left and chain-right isomers (for a 14 × 4 SC) within an energy range between −1.5 eV and +1.5 eV and at distances up to 7 Å above the surface. Perfect agreement between theory and experiment for the whole energy range can be achieved only for a Co atom located at site (7) for the chain-left isomer geometry. For calculated STM topography images for a Co atom located at the other sites listed in Table I we refer the reader to Fig. 16 and Fig. 17. For site (7) we then calculated the electronic properties also for a 26 × 4 SC (size is 103.67 × 27.63 Å, consisting of 1873 atoms) and a 23 × 5 SC (size is 91.74 × 34.54 Å, consisting of 2071 atoms). CG geometry optimization for the chain-left (2) isomer with the Co atom located at site (7) within a 9 × 3 (35.89 × 20.72 Å) SC was performed, similar to the calculations described in Sec. IV B. We used the chain-left (1) and chain-left (2) isomers (see Sec. IV A) for the 26 × 4 SC and 23 × 5 SC, respectively, to keep the Co atom in the center of the SC. Calculations for the 26 × 4 chain-left (1) SC and the 23 × 5 chain-left (2) SC yield identical results.

For our simulations of the STM topography images we have to rely on experimental $z(V_t)$ spectra measured on the Ge(111)2 × 1 surface in order to take into account the dependence of the height z on the tunneling voltage V_t in our calculations. The experimental $z(V_t)$ dependence with an initial height addition of 3 Å[92] was used to determine the height above the Ge(111)2 × 1 surface at which simulated STM images are calculated. For low voltages, i.e., for energies close to E_F, $z(V_t) \simeq 3.7$ Å, while for high voltages above 1 V, $z(V_t) \simeq 6$ Å.

In Fig. 11 we present a series of experimental (inner columns) and calculated (outer columns) STM topography images for the filled (two right columns) and empty (two left columns) state regime within a wide range of tunneling voltages. Calculated STM topography images are obtained for a 23 × 5 SC with chain-left (2) isomer geometry with the Co atom at site (7). Experimental STM topography images are all recorded at the same location. The Co atom is well separated from other Co atoms, implying that there is no influence from neighboring Co atoms (see Sec. III).

As can be seen in Fig. 11, correspondence between the Co-related features in the calculated and the experimental STM topography images is striking for the whole investigated voltage range. Concerning the precise tunneling voltage V_t at which optimum correspondence is observed between theory and experiment there is a minor mismatch. This mismatch exhibits a nonlinear dependence on the applied tunneling voltage for both the filled and empty state regime. At low tunneling voltages the difference in voltage is around 0.1 V for both the empty and filled state regime (see the first row of images in Fig. 11). For higher tunneling voltages, the difference increases to around 0.37 V and 0.23 V for the filled and empty state regime, respectively. Upon more careful

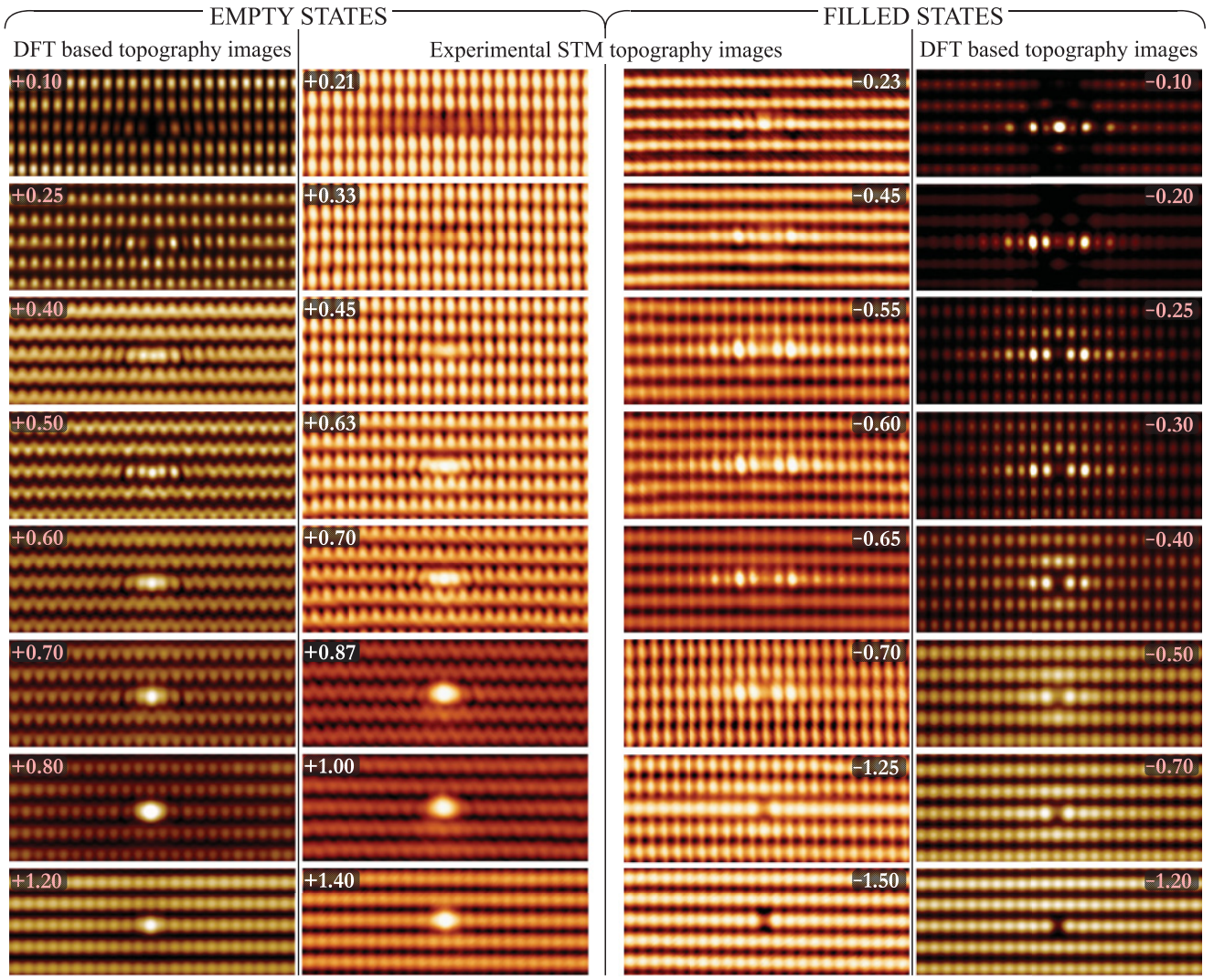

FIG. 11. (Color online) 9.2×3.5 nm^2 experimental empty and filled state STM topography images (inner columns), together with the corresponding calculated DFT-based STM topography images (outer columns) of a single Co atom located in a subsurface 7-member Ge ring, in between the third and fourth atomic layer underneath the Ge(111)2×1 surface. The tunneling voltage V_t is indicated for each image.

comparison, it can be seen that the difference in voltage mainly affects the surrounding Ge(111)2×1 surface and not the Co atom itself. Indeed, maximum contrast related to the Co protrusion appears around $V_t = 0.9 \pm 0.1$ V in both the experimental [Fig. 11 and Fig. 6(a4)] and the calculated STM topography images. Apart from the rather small difference in voltage, there is a very good agreement between the theoretically and experimentally observed electronic features for both the filled and empty state regime.

The results presented in Fig. 11 confirm that the calculated images of the Co/Ge(111) system exhibit all typical features that were observed in the voltage-dependent STM investigation (Sec. III C): (i) The Co-induced strongly perturbed area comprises ± 2 SUCs on the upper π-bonded chain row at moderate and high energies in the empty-state regime; (ii) the perturbation has a mirror symmetry axis along the $[2\bar{1}\bar{1}]$ direction; (iii) the perturbation exhibits a clear asymmetry with respect to the $[01\bar{1}]$ direction; (iv) the Ge(111)2×1 surface exhibits a zigzag structure only at a specific tunneling voltage and this zigzag structure is perturbed near the Co atom.

In the filled-state regime the calculated 1D Co-induced perturbation along the π-bonded chain row exhibits the highest contrast in the -0.25 to -0.35 eV voltage range, whereas experimentally the highest contrast occurs around $eV_t = -0.65 \pm 0.05$ eV [see Fig. 6(b3) and Fig. 11]. At these energies the Co-induced perturbed atomic corrugations along the upper π-bonded chain row in the calculated and experimental STM topography images match very well. At energies below -1.0 eV the Co atom appears as an atomic-size vacancy in the upper π-bonded chain row for both the calculated and experimental STM topography.

In the calculated images the zigzag structure of the Co containing upper π-bonded chain rows is observed at empty-state energy around 0.57 eV (see Fig. 12). On the other hand, this zigzag structure appears around $V_{\text{zigzag}} = 0.85$ eV in the experimental STM images (see Sec. III B). The determination of the angle α in Fig. 12 allows for an easy comparison to Fig. 4(d). It can be seen that apart from a small energy mismatch, the Co-induced perturbation of the calculated zigzag structure again perfectly matches the experimental observation.

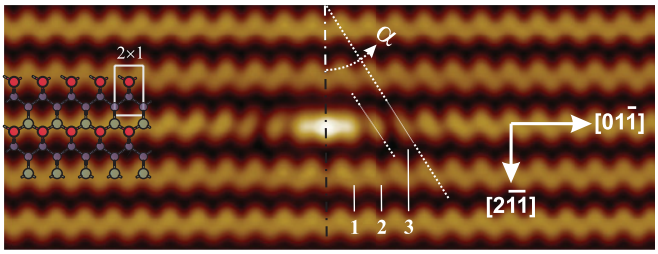

FIG. 12. (Color online) Calculated empty-state STM topography image of a Co atom located at site (7) in the Ge(111)2 × 1 surface. The empty-state energy (0.57 V) is close to the energy for optimum calculated contrast of the zigzag structure of the upper π-bonded chains.

The energy mismatch between the calculated and experimental STM results can be related to the doping of the investigated Ge crystals (p-type Ge crystals with a low dopant concentration are used in this work), which is not included in the DFT modeling. Since the surface and bulk bands shift in energy depending on the type of doping and on the doping level, it can be expected that the Co-induced perturbations shift in energy as well. On the other hand, whereas deposition of 0.032 MLs of Co did not lead to changes of the Ge(111)2 × 1 electronic structures in the experiments, the incorporation of the Co atom in the DFT model may induce a "doping" effect of the Co/Ge(111)2 × 1 system due to the finite size of the SC. For the 23 × 5 SC, the Co/Ge ratio is 1/2071, which corresponds to a heavily doped Ge crystal. As already mentioned in Sec. III B, the precise value of the tunneling voltage V_{zigzag} is found to depend on the semiconductor type and on the doping concentration. For example, heavily doped n-Ge(111)2 × 1 surfaces (phosphor doping level $n_{\text{P}} = 1 \times 10^{19}$ cm^{-3}, surface preparation as described in Sec. II) are found to have $V_{\text{zigzag}} = 0.55$ V, which is in good agreement with the calculated tunneling voltage of 0.57 V.

Finally, we investigated the influence of the doping level on the appearance of the clean Ge(111)2 × 1 surface and the Co/Ge(111)2 × 1 system in experimental STM topography images. As indicated above, it can be expected that the Co-induced perturbations shift in energy, since the surface and bulk bands shift in energy depending on the type of doping and the doping level. In Fig. 13 we present two experimental filled-state STM topography images of a low-doped n-type Ge(111)2 × 1 surface. The Ge crystal was doped by P at a doping level $n_{\text{P}} = 0.5$ to 1.0×10^{15} cm^{-3} ($\rho_{\text{bulk}} \simeq 11$ Ωcm). Surface preparation and Co deposition are performed as described in Sec. II. At low temperatures ($T_{\text{sample}} \simeq 4.5$ K), these samples exhibit a detectable tunneling current in the filled-state regime only at tunneling voltages below −0.8 V. Interestingly, the above described Co-induced perturbations appear at significantly different energies for this low-doped sample. The features observed in Fig. 13(a) for the n-type Ge(111)2 × 1 surface are observed around $V_{\text{t}} = -0.7$ V for the p-type Ge(111)2 × 1 surface (see Fig. 11), corresponding to an energy shift of about 0.7 to 0.8 eV. A similar energy shift can be inferred by comparison of Fig. 13(b) and Fig. 11. The energy shifts between the STM experiments and the DFT calculations in Fig. 11 may therefore be attributed to doping effects. Alternatively, the observed energy shifts may also be related to the intrinsic deficiency of LDA with respect to the quantitative determination of band gap values of semiconductor materials.

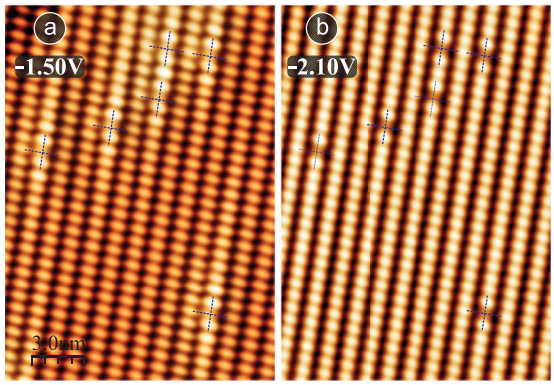

FIG. 13. (Color online) (a), (b) 14.0 × 21 nm^2 experimental filled-state STM images of 6 individual Co atoms for n-type Ge(111)2 × 1 (resistance $\rho_{\text{bulk}} \simeq 11$ Ωcm). The tunneling voltage V_t is indicated for each image. I_t is fixed at 100 pA for (a) and at 500 pA for (b). Blue cross markers indicate identical locations in (a) and (b).

F. Co/Ge(111)2 × 1 electronic properties and Co–Ge bonding characteristics

In this section we discuss the chemical bonds that are formed between the Co atom at site (7) and its surrounding Ge atoms [labeled in Fig. 15(b1)] underneath the Ge(111)2 × 1 surface. The amount of possible chemical bonds can be roughly estimated by relying on a simple analysis of the Co-Ge bond lengths. For a single bond between a Co and a Ge atom the bond length can be estimated as the sum of the Co and Ge covalent radii, which is $r_{\text{c}} = 2.38$ Å. The calculated distances between the Co atom and the neighboring Ge atoms for the 8 × 4 SC equilibrium geometry (see Sec. IV B) are listed in Table II. Among the listed Ge atoms, Ge atoms (2) to (5) are most likely to form a covalent bond with the Co atom. The distances between the Co atom and these Ge atoms are, however, slightly larger (1–2 %) than r_{c}, which can be attributed to the employed LDA (an overestimation of the bond lengths by a few percent is typical for LDA). On the other hand, the calculated Co–Ge(1) distance is significantly larger (around 13%) than r_{c}, implying that the formation of a bond between the Co atom and the Ge(1) up-atom can be excluded.

An estimate of the atomic charges, electron transfer, and covalent interactions between the Co atom at site (7) and the

TABLE II. Calculated distances between the Co atom at site (7) and the neighboring Ge atoms [labeled in Fig. 15(b1)] for the 8 × 4 SC equilibrium geometry.

Co Neighboring Atoms	Co–Ge Distance (Å)
Co–Ge(1)	2.687
Co–Ge(2)	2.404
Co–Ge(3)	2.404
Co–Ge(4)	2.415
Co–Ge(5)	2.243

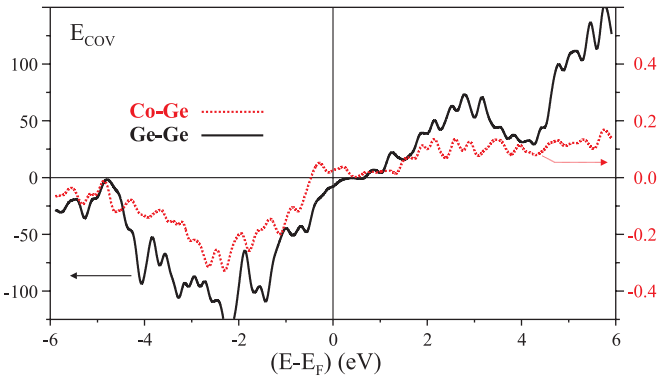

FIG. 14. (Color online) Chemical bonding in terms of the covalent bond energy (E_{COV}) for Ge–Ge bulk and Co–Ge interactions.

neighboring Ge atoms [labeled in Fig. 15(b1); also see Table II] can be obtained more qualitatively from the calculated number of electrons inside the atomic spheres and from the Mulliken populations.[93] The Mulliken electron orbital overlap populations (calculated for the 23 × 5 SC) of Ge atoms (1) to (5) both with [perturbed π-bonded chain row of the Co/Ge(111)2 × 1 system] and without [unperturbed π-bonded chain row of the Ge(111)2 × 1 surface] the Co atom are given in parts (A) and (B), respectively, of Table III. The (unperturbed) bulk atoms Ge(4′) and Ge(5′) have four Ge–Ge covalent bonds, with an electron orbital overlap population around 0.40 ± 0.01 e/bond (sp^3 hybridization). On the other hand, up-atom Ge(1′) and down-atoms Ge(2′,3′) have only three covalent bonds (sp^2 hybridization): A fourth bond is absent or at least strongly reduced (Mulliken overlap populations are less than 22% of the Ge–Ge bulk covalent bond). Co-induced changes in the Mulliken overlap population of the neighboring Ge atoms and the atom population can be traced by comparison of part (A) of Table III to part (B). The calculations reveal that no significant charge redistribution between the Co atom and the surface and bulk Ge atoms occurs; i.e., the electron population of the Co atom remains close to that of a neutral Co atom (9.043 e). The Co atom exhibits four covalent bonds with Mulliken overlap populations that are 56 to 60% of the Ge–Ge bulk covalent bond. There exists a weak interaction with the Ge(1) up-atom

TABLE III. (A) Mulliken overlap population and electron population of the perturbed Ge atoms neighboring the embedded Co atom at site (7) and (B) of the unperturbed Ge atoms in the absence of the Co atom [ideal Ge(111)2 × 1 surface]. Ge atoms are numbered according to Fig. 15(b1) and Table II.

(A) Co/Ge(111)2 × 1 Bond (atom–atom)	Ge(1)	Ge(2)	Ge(3)	Ge(4)	Ge(5)
Ge–Ge	0.368	0.444	0.396	0.368	0.228
Ge–Ge	0.394	0.394	0.445	0.401	0.356
Ge–Ge	0.396	0.409	0.408	0.228	0.401
Ge–Ge		0.067	0.065	0.401	0.353
Co–Ge	0.120	0.241	0.239	0.224	0.231
Electron pop.	4.205	3.891	3.889	3.943	3.884
(B) Ideal (2 × 1) Bond (atom–atom)	**Ge(1′)**	**Ge(2′)**	**Ge(3′)**	**Ge(4′)**	**Ge(5′)**
Ge–Ge	0.412	0.475	0.475	0.412	0.395
Ge–Ge	0.476	0.476	0.456	0.402	0.406
Ge–Ge	0.475	0.435	0.435	0.395	0.405
Ge–Ge		0.089	0.089	0.402	0.406
Electron pop.	4.172	3.882	3.859	3.982	3.961

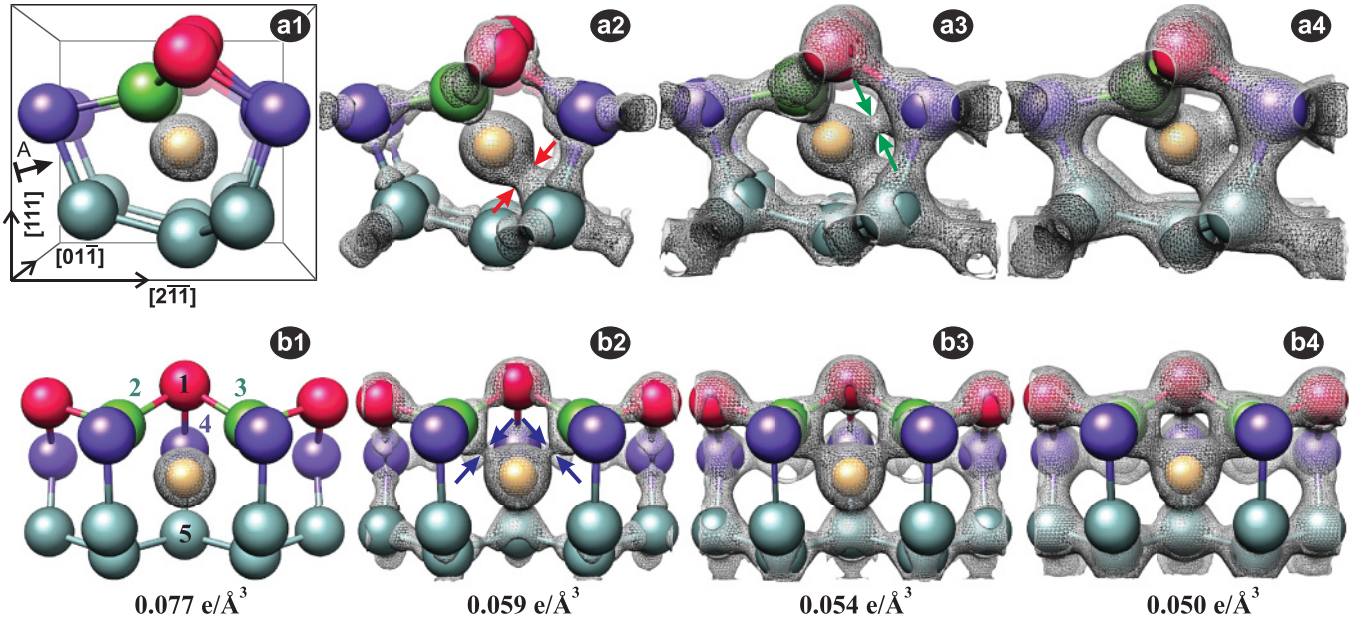

FIG. 15. (Color online) 3D isosurface charge density $\rho(x,y,z)$ plots of the Co/Ge(111)2 × 1 system (chain-left isomer) with the Co atom located inside the big 7-member Ge ring below the surface. Viewpoint is along the [01$\bar{1}$] direction for (a1) to (a4) and along the direction indicated by the arrow A in (a1) for (b1) to (b4). The charge density ρ (e/Å^3) isovalues for (a1), (a2), (a3), and (a4) are the same as the ones for (b1), (b2), (b3), and (b4), respectively, and are indicated at the bottom of the latter parts of the figure.

as well [see Table III, part (A)]. Because of the very low overlap population (30% of Ge–Ge bulk bond) and the very weak charge transfer between Co and Ge(1), however, the interaction between the Co and Ge(1) up-atom should not be considered as a fifth covalent bond.

The energy of the covalent Co-Ge bonds can be estimated as the total energy difference between a Co atom that is "bonded" [Co atom located at site (7)] or "not bonded" to the Ge lattice. Calculations for the "not bonded" case were performed for a 4×2 SC with the Co atom placed 4 Å above the Ge surface. The total energy difference is found to be 8.4 ± 0.3 eV. Considering four Co–Ge bonds as discussed above, the (average) energy of a single Co–Ge bond is hence $E_{\mathrm{Co-Ge}} = 2.1$ eV, which is significantly lower than the energy of the covalent Ge–Ge bond ($E_{\mathrm{Ge-Ge}} = 3.71$ eV).

The analysis of the bond lengths and the Mulliken overlap populations are indicative of rather weak Co–Ge bonds, which can also be concluded from our experimental observation that Co atoms diffuse even at lower temperatures.[62] More precisely, in spite of the low sample temperature ($T_{\mathrm{sample}} \leqslant 80$ K) during Co deposition, the majority (around 87%) of the Co atoms diffuse along π-bonded chain rows to surface and subsurface defects (including DBs, MASs, and subsurface Ga impurities), which can be related to the weak Co–Ge bonds. The remaining 13% can be retrieved as individual (subsurface) Co atoms at the cold Ge surface and they diffuse as well to surface and subsurface defects after warming the substrate up to room temperature. For a more detailed discussion we refer the reader to Ref. 62.

The chemical bonding mechanism between the Co and Ge atoms involved in the DFT electronic structure calculations can be investigated in more detail by evaluating the crystal orbital overlap population/Hamiltonian population (COOP/COHP).[94,95] We have used an alternative COOP/COHP-based approach that allows us to calculate the relevant physical quantities independent of the choice of zero of the potential by relying on the so-called "covalent bond energy" (E_{COV}).[96] COOP and E_{COV} calculations are known to yield similar results, while the COOP method generally overestimates the magnitude of the antibonding states when defined within a plane-wave basis set.[97] Figure 14 presents our E_{COV} calculation for the Co–Ge and Ge–Ge bulk interactions in an energy range of 12 eV around the Fermi level. Note that the E_{COV} values (y ordinate) are plotted without any units and can only be interpreted qualitatively. Negative, positive, and zero values of E_{COV} correspond to bonding, antibonding, and nonbonding interactions, respectively. The E_{COV} spectra confirm the stability of the Co/Ge system. Strong bonding interactions exist for Ge–Ge from the bottom of the VB up to the Fermi level, while for the Co–Ge a strong bonding interaction is found only up to around -0.3 eV. Between -0.3 eV and the Fermi level, Co–Ge antibonding interactions occur, which may explain the experimentally observed thermal instability of the Co/Ge system (the covalent Co–Ge bonds are weaker than the Ge–Ge bulk bonds).

Finally, we calculated charge electron density maps to visualize the Co–Ge bonds. In Fig. 15 we present isosurface maps of the spatial electron charge density $\rho(x,y,z)$ for isosurface values ranging from 0.077 $e/$Å^3 down to 0.050 $e/$Å^3. High electron densities related to the Ge–Ge covalent bonds gradually appear above 0.059 $e/$Å^3 in Figs. 15(a2) and 15(b2) to Figs. 15(a4) and 15(b4). Moreover, zones of high electron localization between the Co atom and the surrounding Ge atoms can be observed. A zone of high electron localization exists between the Co atom and the Ge(5) atom in Fig. 15(a2) (indicated by red arrows). Two additional symmetrical zones of high electron localization can be observed between the Co atom and the Ge(2) and Ge(3) down-atoms in Fig. 15 (b2) (indicated by the blue arrows). A fourth Co–Ge bond can be related to the high electron localization zone between the Co atom and the Ge(4) atom in Fig. 15(a3) (indicated by the green arrows). As could be expected from our above analysis, there occurs no high electron localization zone between the Co atom and the up-atom Ge(1), which additionally confirms that both atoms are not bonded. The findings related to the bond lengths, the Mulliken overlap populations, and the E_{COV} calculations are hence in agreement with the isosurface charge density maps. We therefore conclude that the Co atom forms a bond with four neighboring Ge atoms, corresponding to a Co^{4+} valence state and a $3d^5$ electron configuration. It is known that Co has a wide range of valence states due to its various spin configurations, implying that Co^{4+}, i.e., $3d^5$, ions can exist in several spin configurations.[98,99] An extension of our DFT model for the embedding of a Co atom in the Ge lattice by including spin-dependent calculations will be a topic of future research.

V. CONCLUSION

Noninvasive embedding of individual Co atoms into clean Ge(111)2×1 surfaces was systematically investigated by means of STM experiments and DFT calculations. STM experiments indicate that these Co atoms appear exclusively at upper π-bonded chain rows after deposition on cold Ge(111)2×1 surfaces ($T_{\mathrm{sample}} \leqslant 80$ K). Analysis of the voltage-dependent STM images reveals that all adsorbed Co atoms induce an identical anisotropic electronic perturbation of the surrounding Ge surface and clear 1D confinement along π-bonded chains. Relying on DFT-based calculations we demonstrated that the energetically most favorable position of a Co atom is attained by penetration into the Ge(111)2×1 surface. The Co atom occupies a quasistationary position within the big 7-member Ge ring of the Ge(111)2×1 reconstruction in between the third and fourth atomic layer beneath the surface. The embedded Co atom induces an electronic asymmetry of the π-bonded chain with respect to the $[01\bar{1}]$ direction, which allows us to determine that the Ge(111)2×1 surface reconstruction of all investigated Ge samples consists of domains with chain-left geometry exclusively. Calculated STM images based on our DFT approach match very well the experimental STM images of the Co/Ge(111)2×1 system within the investigated range of tunneling voltages. Finally, DFT-based calculations of the Co–Ge bond strength reveal the formation of four covalent bonds, corresponding to a Co^{4+} valence state and a $3d^5$ electron configuration. Our findings open interesting perspectives for investigations of subsurface 1D (nanowires) and 2D (islands) nanostructures that are expected to form at a higher coverage of Co on Ge(111).

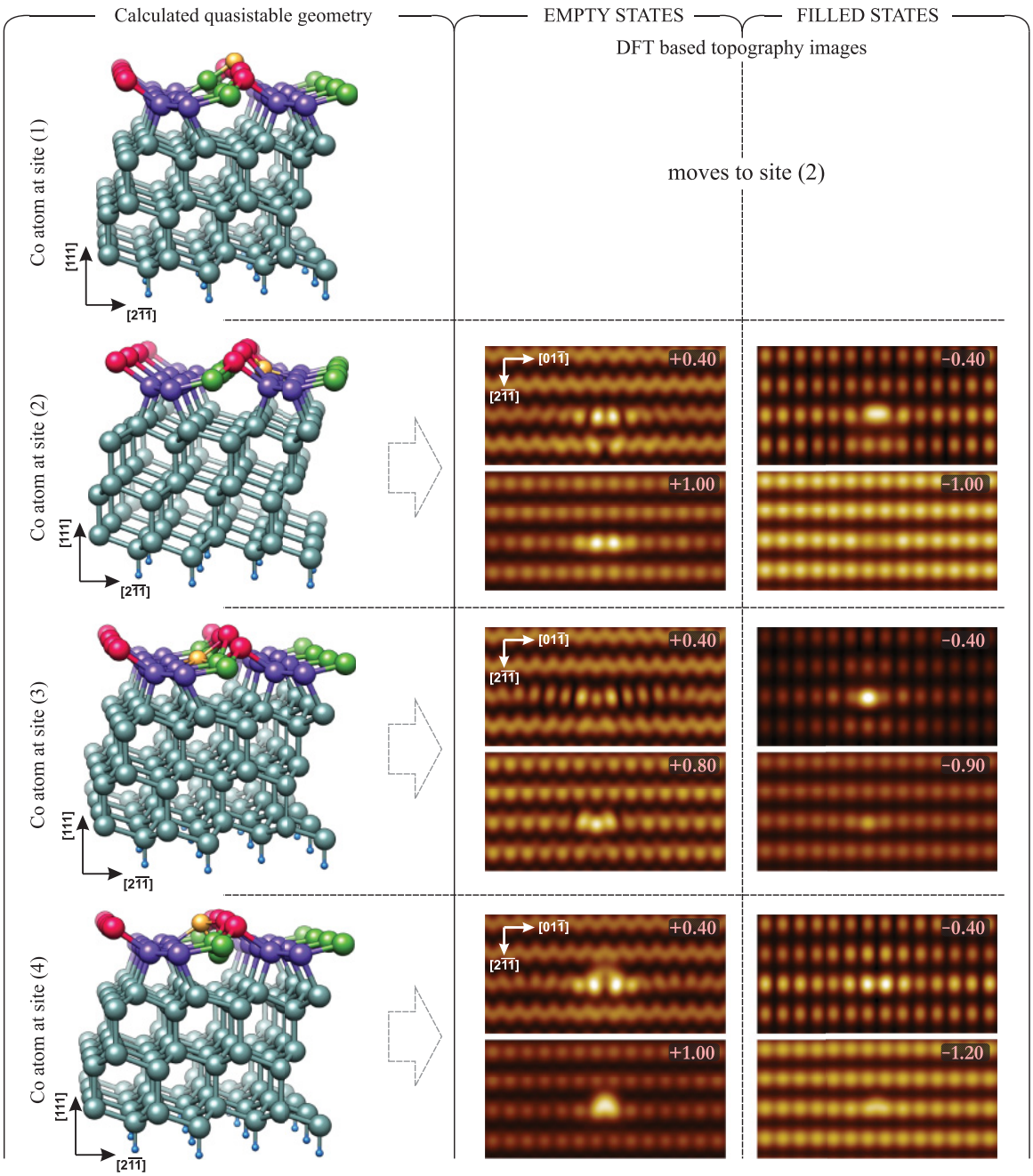

FIG. 16. (Color online) Left panel: Calculated quasistable geometries (within the 4×2 SC) for Co sites (1)–(4) (see Table I) on the Ge(111)2×1 surface. Right panel: Calculated STM topography images for the filled (right column) and empty (left column) state regime. The images are obtained for a 14×4 SC with chain-left isomer geometry and with the Co atom located as illustrated in the corresponding left panel. The tunneling voltage V_t is indicated for each image.

ACKNOWLEDGMENTS

The research in Moscow has been supported by Russian Foundation for Basic Research (RFBR) grants and by the computing facilities of the M. V. Lomonosov Moscow State University (MSU) Research Computing Center. The research in Leuven has been supported by the Research Foundation - Flanders (FWO, Belgium) as well as by the Belgian Interuniversity Attraction Poles (IAP) and the Flemish Concerted Action (GOA) research programs. K.S. acknowledges support as a postdoctoral researcher of the FWO.

APPENDIX: QUASISTABLE Co ADSORPTION SITES

In this appendix we present the results of our calculations for the quasistable Co absorption sites (1), (2), (3), (4), (5), (6), (8), and (9) that were discussed in Sec. IV B (see Table I). In Fig. 16 and Fig. 17 (left panel) we present a 3D ball-and-stick model view of the relaxed Ge(111)2×1 surface for all possible quasistable Co atom sites [except for site (7)] that were identified for the chain-left isomer geometry for a 4×2 SC. The numbers of the Co atom sites in Figs. 16 and 17 correspond to the numbers given in Table I (first column).

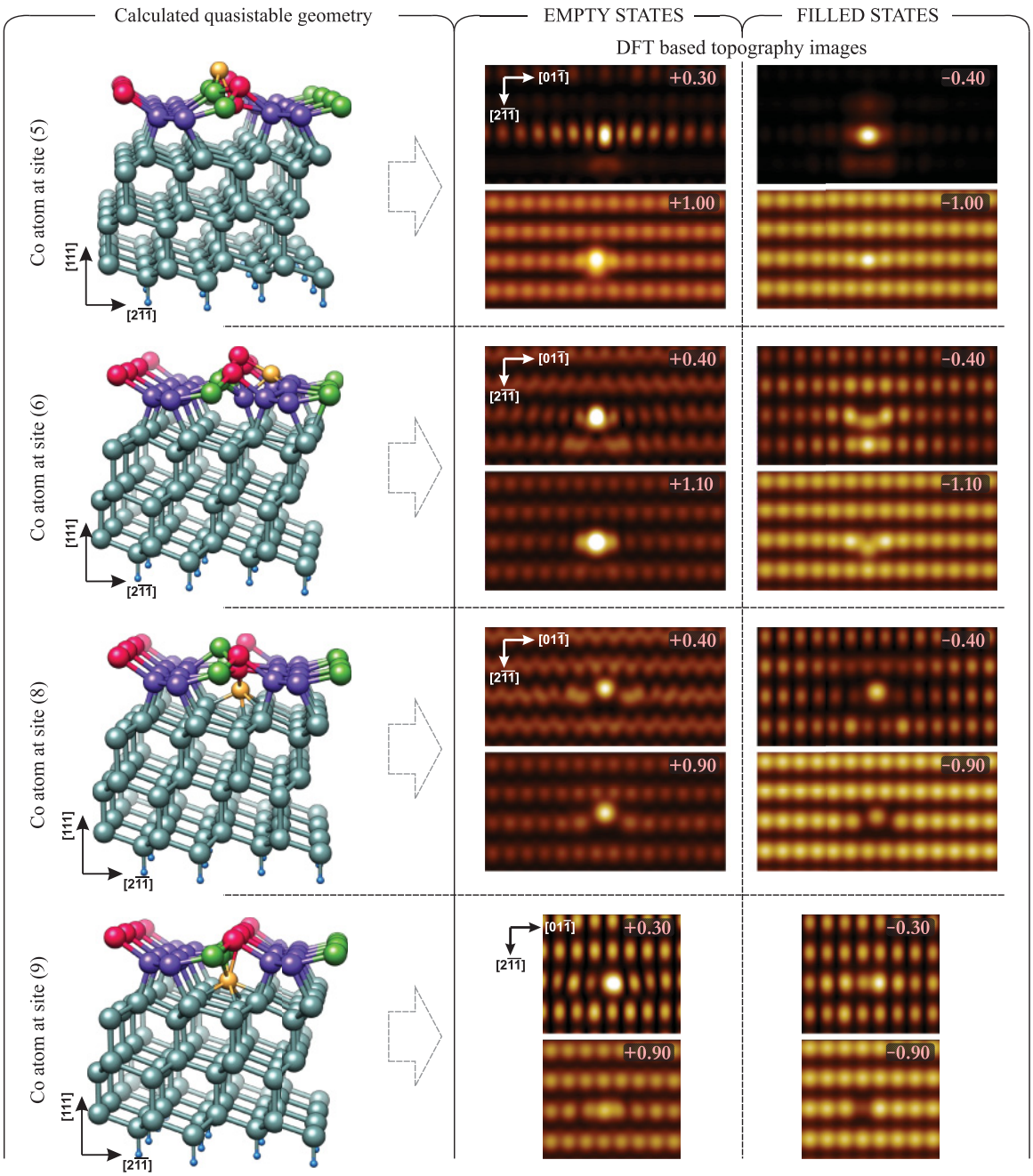

FIG. 17. (Color online) Left panel: Calculated quasistable geometry (within the 4 × 2 SC) for Co sites (5), (6), (8), and (9) (see Table I) on [(5) and (6)] and underneath [(8) and (9)] the Ge(111)2 × 1 surface. Right panel: Calculated STM topography images for the filled (right column) and empty (left column) state regime. The images are obtained for a 14 × 4 SC [8 × 4 SC for the Co at site (9)] with chain-left isomer geometry and with the Co atom located as illustrated in the corresponding left panel. The tunneling voltage V_t is indicated for each image.

In Fig. 16 and Fig. 17 (right panel) we present a series of DFT-based calculated scanning tunneling microscopy topography images for the filled (right column) and empty (left column) state regime at the indicated tunneling voltages. The DFT-based simulations of the STM topography images are obtained as described in Sec. IV E. Calculated STM topography images are obtained for a 14 × 4 SC for all sites [except for site (9), for which a 8 × 4 SC is used] with chain-left isomer geometry and with the Co atom located as illustrated in the corresponding left panel.

*mda@spmlab.ru
†koen.schouteden@fys.kuleuven.be

[1] P. Bhattacharya, S. Ghosh, and A. Stiff-Roberts, Annu. Rev. Mater. Res. **34**, 1 (2004).
[2] Y.-H. Kuo, Y. K. Lee, Y. Ge, S. Ren, J. E. Roth, T. I. Kamins, D. A. B. Miller, and J. S. Harris, Nature (London) **437**, 1334 (2005).
[3] A. C. Whalley, M. L. Steigerwald, X. Guo, and C. Nuckolls, J. Am. Chem. Soc. **129**, 12590 (2007).

[4] A. Grigoriev, J. Sköldberg, G. Wendin, and Z. Crljen, Phys. Rev. B **74**, 045401 (2006).

[5] J. J. Parks, A. R. Champagne, T. A. Costi, W. W. Shum, A. N. Pasupathy, E. Neuscamman, S. Flores-Torres, P. S. Cornaglia, A. A. Aligia, C. A. Balseiro, G. K.-L. Chan, H. D. Abruna, and D. C. Ralph, Science **328**, 1370 (2010).

[6] G. A. Prinz, Phys. Today **48**(4), 58 (1995).

[7] M. B. Haider, J. L. Pitters, G. A. DiLabio, L. Livadaru, J. Y. Mutus, and R. A. Wolkow, Phys. Rev. Lett. **102**, 046805 (2009).

[8] K. Y. Tan, K. W. Chan, M. Mttnen, A. Morello, C. Yang, J. van Donkelaar, A. Alves, J.-M. Pirkkalainen, D. N. Jamieson, R. G. Clark, and A. S. Dzurak, Nano Lett. **10**, 11 (2009).

[9] H. Bracht, S. Schneider, J. N. Klug, C. Y. Liao, J. L. Hansen, E. E. Haller, A. N. Larsen, D. Bougeard, M. Posselt, and C. Wündisch, Phys. Rev. Lett. **103**, 255501 (2009).

[10] C. Wundisch, M. Posselt, B. Schmidt, V. Heera, T. Schumann, A. Mucklich, R. Grotzschel, W. Skorupa, T. Clarysse, E. Simoen, and H. Hortenbach, Appl. Phys. Lett. **95**, 252107 (2009).

[11] S. M. Sze and J. C. Irvin, Solid-State Electron. **11**, 599 (1968).

[12] M. L. Lee, E. A. Fitzgerald, M. T. Bulsara, M. T. Currie, and A. Lochtefeld, J. Appl. Phys. **97**, 011101 (2005).

[13] C. W. Leitz, M. T. Currie, M. L. Lee, Z.-Y. Cheng, D. A. Antoniadis, and E. A. Fitzgerald, J. Appl. Phys. **92**, 3745 (2002).

[14] C. Claeys and E. Simoen, *Germanium-Based Technologies—From Materials to Devices* (Elsevier, Amsterdam, 2007) .

[15] J. Appenzeller, Y.-M. Lin, J. Knoch, and P. Avouris, Phys. Rev. Lett. **93**, 196805 (2004).

[16] C. O. Chui, K. Gopalakrishnan, P. B. Griffin, J. D. Plummer, and K. C. Saraswat, Appl. Phys. Lett. **83**, 3275 (2003).

[17] S. M. Reimann and M. Manninen, Rev. Mod. Phys. **74**, 1283 (2002).

[18] N. Nilius, T. M. Wallis, and W. Ho, Science **297**, 1853 (2002).

[19] J. Wang, M. Li, and E. I. Altman, Phys. Rev. B **70**, 233312 (2004).

[20] K. Schouteden, E. Lijnen, D. A. Muzychenko, A. Ceulemans, L. F. Chibotaru, P. Lievens, and C. V. Haesendonck, Nanotechnology **20**, 395401 (2009) .

[21] L. P. Kouwenhoven, D. G. Austing, and S. Tarucha, Rep. Prog. Phys. **64**, 701 (2001) .

[22] S. A. Wolf, D. D. Awschalom, R. A. Buhrman, J. M. Daughton, S. von Molnár, M. L. Roukes, A. Y. Chtchelkanova, and D. M. Treger, Science **294**, 1488 (2001).

[23] I. Žutić, J. Fabian, and S. Das Sarma, Rev. Mod. Phys. **76**, 323 (2004).

[24] C. Zeng, W. Zhu, S. C. Erwin, Z. Zhang, and H. H. Weitering, Phys. Rev. B **70**, 205340 (2004).

[25] G. Profeta, S. Picozzi, A. Continenza, and C. Franchini, Phys. Rev. B **70**, 155307 (2004).

[26] N. Oncel, A. van Houselt, J. Huijben, A.-S. Hallbäck, O. Gurlu, H. J. W. Zandvliet, and B. Poelsema, Phys. Rev. Lett. **95**, 116801 (2005).

[27] J. Schäfer, D. Schrupp, M. Preisinger, and R. Claessen, Phys. Rev. B **74**, 041404 (2006).

[28] A. A. Stekolnikov, F. Bechstedt, M. Wisniewski, J. Schäfer, and R. Claessen, Phys. Rev. Lett. **100**, 196101 (2008).

[29] A. A. Stekolnikov, J. Furthmüller, and F. Bechstedt, Phys. Rev. B **78**, 155434 (2008).

[30] D. E. P. Vanpoucke and G. Brocks, Phys. Rev. B **81**, 085410 (2010).

[31] S. Sauer, F. Fuchs, F. Bechstedt, C. Blumenstein, and J. Schäfer, Phys. Rev. B **81**, 075412 (2010).

[32] A. van Houselt, M. Fischer, B. Poelsema, and H. J. W. Zandvliet, Phys. Rev. B **78**, 233410 (2008).

[33] K. Tomatsu, K. Nakatsuji, T. Iimori, and F. Komori, Surf. Sci. **601**, 1736 (2007).

[34] M. Fischer, A. van Houselt, D. Kockmann, B. Poelsema, and H. J. W. Zandvliet, Phys. Rev. B **76**, 245429 (2007).

[35] J. Wang, M. Li, and E. I. Altman, J. Appl. Phys. **100**, 113501 (2006).

[36] J. R. Lince, J. G. Nelson, and R. S. Williams, J. Vac. Sci. Tech. B **1**, 553 (1983).

[37] L. H. Chan and E. I. Altman, Phys. Rev. B **66**, 155339 (2002).

[38] S. S. P. Parkin, Phys. Rev. Lett. **71**, 1641 (1993).

[39] J. S. Tsay, Y. D. Yao, K. C. Wang, W. C. Cheng, and C. S. Yang, Surf. Sci. **507–510**, 498 (2002).

[40] P. Ryan, R. P. Winarski, D. J. Keavney, J. W. Freeland, R. A. Rosenberg, S. Park, and C. M. Falco, Phys. Rev. B **69**, 054416 (2004).

[41] J. S. Tsay, H. Y. Nieh, Y. D. Yao, Y. T. Chen, and W. C. Cheng, Surf. Sci. **566–568**, 226 (2004).

[42] J. S. Tsay, C. W. Su, C. H. Hwang, and Y. D. Yao, J. Vac. Sci. Tech. A **23**, 781 (2005).

[43] H. W. Chang, J. S. Tsay, Y. L. Chiou, K. T. Huang, W. Y. Chan, and Y. D. Yao, J. Appl. Phys. **99**, 08J705 (2006).

[44] J. S. Tsay, H. Y. Nieh, C. S. Yang, Y. D. Yao, and T. S. Chin, J. Appl. Phys. **93**, 8728 (2003).

[45] J. Tsay, H. Nieh, Y. Yao, and T. Chin, J. Magn. Magn. Mat. **282**, 78 (2004).

[46] C. Su, J. Tsay, and Y. Yao, J. Magn. Magn. Mat. **304**, e41 (2006).

[47] J. V. Barth, H. Brune, G. Ertl, and R. J. Behm, Phys. Rev. B **42**, 9307 (1990).

[48] K. Schouteden, E. Lijnen, E. Janssens, A. Ceulemans, L. F. Chibotaru, P. Lievens, and C. V. Haesendonck, New J. Phys. **10**, 043016 (2008) .

[49] I. Horcas, R. Fernandez, J. M. Gomez-Rodriguez, J. Colchero, J. Gomez-Herrero, and A. M. Baro, Rev. Sci. Inst. **78**, 013705 (2007) .

[50] J. E. Northrup and M. L. Cohen, Phys. Rev. B **27**, 6553 (1983).

[51] K. C. Pandey, Phys. Rev. Lett. **47**, 1913 (1981).

[52] R. M. Feenstra and A. J. Slavin, Surf. Sci. **251–252**, 401 (1991).

[53] R. M. Feenstra, G. Meyer, F. Moresco, and K. H. Rieder, Phys. Rev. B **64**, 081306 (2001).

[54] Y. Einaga, H. Hirayama, and K. Takayanagi, Phys. Rev. B **57**, 15567 (1998).

[55] D. A. Muzychenko, S. V. Savinov, V. N. Mantsevich, N. S. Maslova, V. I. Panov, K. Schouteden, and C. Van Haesendonck, Phys. Rev. B **81**, 035313 (2010).

[56] H. M. Guo, H. W. Liu, Y. L. Wang, H. J. Gao, H. X. Shang, Z. W. Liu, H. M. Xie, and F. L. Dai, Nanotech. **15**, 991 (2004) .

[57] F. Bechstedt, A. A. Stekolnikov, J. Furthmüller, and P. Käckell, Phys. Rev. Lett. **87**, 016103 (2001).

[58] K. Kobayashi, Phys. Rev. B **68**, 075308 (2003).

[59] J. M. Nicholls, G. V. Hansson, R. I. G. Uhrberg, and S. A. Flodström, Phys. Rev. B **27**, 2594 (1983).

[60] J. M. Nicholls, G. V. Hansson, U. O. Karlsson, R. I. G. Uhrberg, R. Engelhardt, K. Seki, S. A. Flodström, and E. E. Koch, Phys. Rev. Lett. **52**, 1555 (1984).

[61] J. M. Nicholls, P. Maartensson, and G. V. Hansson, Phys. Rev. Lett. **54**, 2363 (1985).

[62] D. A. Muzychenko, K. Schouteden, V. I. Panov, and C. Van Haesendonck, e-print arXiv:1201.0735.

[63]S. Nie, R. M. Feenstra, J. Y. Lee, and M.-H. Kang, J. Vac. Sci. Tech. A **22**, 1671 (2004).
[64]T. Trappmann, C. Surgers, and H. v. Lohneysen, Appl. Phys. A **68**, 167 (1999).
[65]J. K. Garleff, M. Wenderoth, R. G. Ulbrich, C. Sürgers, and H. v. Löhneysen, Phys. Rev. B **72**, 073406 (2005).
[66]J. K. Garleff, M. Wenderoth, R. G. Ulbrich, C. Sürgers, H. v. Löhneysen, and M. Rohlfing, Phys. Rev. B **76**, 125322 (2007).
[67]F. J. Himpsel, P. M. Marcus, R. Tromp, I. P. Batra, M. R. Cook, F. Jona, and H. Liu, Phys. Rev. B **30**, 2257 (1984).
[68]R. M. Tromp, L. Smit, and J. F. van der Veen, Phys. Rev. B **30**, 6235 (1984).
[69]O. L. Alerhand, D. C. Allan, and E. J. Mele, Phys. Rev. Lett. **55**, 2700 (1985).
[70]J. E. Northrup, M. S. Hybertsen, and S. G. Louie, Phys. Rev. Lett. **66**, 500 (1991).
[71]N. Takeuchi, A. Selloni, A. I. Shkrebtii, and E. Tosatti, Phys. Rev. B **44**, 13611 (1991).
[72]M. Rohlfing, M. Palummo, G. Onida, and R. Del Sole, Phys. Rev. Lett. **85**, 5440 (2000).
[73]H. Hirayama, N. Sugihara, and K. Takayanagi, Phys. Rev. B **62**, 6900 (2000).
[74]W. Kohn and L. J. Sham, Phys. Rev. **140**, A1133 (1965).
[75]J. P. Perdew and A. Zunger, Phys. Rev. B **23**, 5048 (1981).
[76]P. Ordejón, E. Artacho, and J. M. Soler, Phys. Rev. B **53**, R10441 (1996).
[77]D. Sánchez-Portal, P. Ordejón, E. Artacho, and J. M. Soler, Int. J. Quant. Chem. **65**, 453 (1997).
[78]J. M. Soler, E. Artacho, J. D. Gale, A. García, J. Junquera, P. Ordejón, and D. Sánchez-Portal, J. Phys. Condens. Matter **14**, 2745 (2002).
[79]N. Troullier and J. L. Martins, Phys. Rev. B **43**, 1993 (1991).
[80]B. P. Uberuaga, M. Leskovar, A. P. Smith, H. Jónsson, and M. Olmstead, Phys. Rev. Lett. **84**, 2441 (2000).
[81]D.-S. Lin, T. Miller, and T.-C. Chiang, Phys. Rev. B **45**, 11415 (1992).
[82]O. Gurlu, H. J. W. Zandvliet, B. Poelsema, S. Dag, and S. Ciraci, Phys. Rev. B **70**, 085312 (2004).
[83]G. A. Smith, L. Luo, S. Hashimoto, W. M. Gibson, and N. Lewis, J. Vac. Sci. Tech. A **7**, 1475 (1989).
[84]T. Asano, N. Uetake, and K. Suzuki, J. Nucl. Sci. Tech. **29**, 1194 (1992).
[85]P. R. Miller, *Atomic and Molecular Beam Methods* (Oxford University Press, Oxford, 1988), p. 14.
[86]K. L. Chopra, *Thin Film Phenomenona* (McGraw-Hill, New York, 1969) .
[87]N. Uetake, T. Asano, and K. Suzuki, Rev. Sci. Inst. **62**, 1942 (1991).
[88]J. Tersoff and D. R. Hamann, Phys. Rev. Lett. **50**, 1998 (1983).
[89]J. Tersoff and D. R. Hamann, Phys. Rev. B **31**, 805 (1985).
[90]O. Paz, I. Brihuega, J. M. Gómez-Rodríguez, and J. M. Soler, Phys. Rev. Lett. **94**, 056103 (2005).
[91]M. Rohlfing, R. Temirov, and F. S. Tautz, Phys. Rev. B **76**, 115421 (2007).
[92]C. K. Shih, R. M. Feenstra, and G. V. Chandrashekhar, Phys. Rev. B **43**, 7913 (1991).
[93]R. S. Mulliken, J. Chem. Phys. **23**, 1833 (1955).
[94]R. Hoffmann, J. Phys. Condens. Matter **5**, A1 (1993).
[95]R. Dronskowski and P. E. Bloechl, J. Phys. Chem. **97**, 8617 (1993).
[96]G. Bester and M. Fähnle, J. Phys. Condens. Matter **13**, 11541 (2001).
[97]V. Paul-Boncour and S. F. Matar, Phys. Rev. B **70**, 184435 (2004).
[98]K. D. Sen and L. J. Bartolotti, Phys. Rev. A **45**, 2076 (1992).
[99]P. Ravindran, P. A. Korzhavyi, H. Fjellvåg, and A. Kjekshus, Phys. Rev. B **60**, 16423 (1999).